

The structure of diatom communities constrains biogeochemical properties in surface waters of the Southern Ocean (Kerguelen Plateau)

Lafond Augustin ^{1,*}, Leblanc Karine ¹, Legras Justine ¹, Cornet Véronique ¹, Quéguiner Bernard ¹

¹ Aix-Marseille University, Université de Toulon, CNRS, IRD, MIO, UM 110, 13288, Campus de Luminy, 163 avenue de Luminy, Marseille 13288, France

* Corresponding author : Augustin Lafond, email address : augustin.lafond@gmail.com

Abstract :

In the context of climate change, understanding the ecological processes controlling the functioning and the efficiency of the biological pump is of primary importance. Plankton community structure and species-specific properties are often invoked as likely to affect biogeochemistry and the export of organic and biogenic material to the ocean interior. Although a major player in this respect, diatoms are still viewed as a single functional type whose diversity is generally overlooked. Here we examine that question, building on the results achieved during the MOBYDICK expedition, which occurred in the vicinity of the Kerguelen Islands (Southern Ocean) in late summer, a time window corresponding to the demise of the annually recurrent phytoplankton blooms already known to be controlled by iron availability. The Si/C/N stoichiometry of the particulate matter was studied in conjunction with the different diatom community structures, their physiological states, as well as their species-specific carbon contents and silicification degrees. Our results show that diatoms outside the iron-fertilized plateau were more heavily silicified, due to the combined effects of both taxonomic composition of the resident community and a direct physiological response to iron stress, resulting in higher Si:C elemental ratios in diatoms as well as in the bulk particulate matter. Despite low silicic acid concentrations, large chains of weakly silicified *Corethron inerme* were able to grow in the upper mixed layer above the plateau, while in adjacent high nutrient low chlorophyll (HNLC) waters, communities were dominated by *Fragilariopsis* spp., *Cylindrotheca closterium* and the centric genera *Actinocyclus*/*Thalassiosira* spp. Depth was also an important factor shaping diatom communities, with the presence of a deep and inactive assemblage located within the pycnocline gradient, both on- and off-plateau, which likely resulted from the differential sinking and accumulation of species previously grown at the surface. In HNLC waters, below the mixed layer, detrital frustules of the heavily silicified species *Fragilariopsis kerguelensis* carried mostly Si, while above the plateau, *Eucampia antarctica* and *Chaetoceros* spp. (resting spores and vegetative stages) were efficient vectors of both Si and C to the deeper layers. Our study shows that the stoichiometry of the biological pump cannot be considered solely as a simple response to a single limiting factor (here iron) highlighting the importance of a species-centered approach in order to finely resolve biogeochemical fluxes and improve our understanding of the biological pump.

Highlights

► A distinct diatom community was growing despite low $[\text{Si}(\text{OH})_4]$ above the Fe-fertilized plateau. ► A deep and inactive diatom community was systematically found within the pycnocline gradient. ► In HNLC waters, diatoms were more heavily silicified and exhibited higher Si:C ratios. ► In HNLC waters, detrital frustules of *Fragilariopsis kerguelensis* carried mostly Si below the ML. ► Above the plateau, *Chaetoceros* spp. vegetative cells and spores carried Si and C below the ML.

Keywords : Southern Ocean, Kerguelen Plateau, Diatoms, Community structure, Biological pump

1 Introduction

The Southern Ocean (SO) is a major sink for anthropogenic CO₂ and plays an important role in redistributing heat and nutrients at the global scale (Sarmiento et al., 2004; Sallée et al., 2012; Takahashi et al., 2012; Frölicher et al., 2015). It is also the largest High Nutrient Low Chlorophyll (HNLC) area, and as such its surface waters are characterized by low phytoplankton biomass, despite elevated macronutrient concentrations. This paradox has been solved in the early 1990s when dissolved iron was identified as a potentially strong limiting factor for primary production (Martin, 1990; "The Iron Hypothesis"). In contrast to HNLC waters, highly productive, naturally iron fertilized blooms are observed in discrete areas of the SO, located downstream of island systems such as the Kerguelen Plateau (Blain et al., 2007), Crozet Islands (Pollard et al., 2009) and South Georgia (Whitehouse et al., 1996; Korb and Whitehouse, 2004; Korb et al., 2008). In these so called "natural laboratories", blooms are dominated by siliceous diatoms, and C export is 2-3 times higher than in surrounding Fe-limited areas (Morris et al., 2007; Savoye et al., 2008; Planchon et al., 2015) which are typically dominated by autotrophic nanoplankton (Kopczyńska et al., 1998; Uitz et al., 2009; Lasbleiz et al., 2016). Due to their large sizes, and the ballasting effect of their frustule, diatoms are classically considered as efficient vector of C export (Buesseler, 1998; Armstrong et al., 2002). Throughout the productive season, they progressively consume Si(OH)₄ which becomes limiting in summer, leading to the termination of the bloom (Boyd, 2002; Leblanc et al., 2005; Nelson et al., 2001; Franck et al., 2000).

However, the discovery of High Biomass Low Export ecosystems dominated by diatoms (Lam and Bishop, 2007), and later on, the recurrent observation of an inverse relationship between primary production and export efficiency in the Southern Ocean challenged our understanding of the carbon biological pump (Maiti et al., 2013; Henson et al., 2019). Plankton community structure and species-specific properties can strongly influence the transfer of biogenic minerals (e.g. Si) and organic matter (e.g. C, N etc.) to the ocean interior (Salter et al., 2012; Assmy et al., 2013; Quéguiner, 2013; Rembauville et al., 2015b, 2016; Tréguer et al., 2018; Arteaga et al., 2019). This is particularly true for diatoms which exhibit a

wide range of size and biovolumes (Leblanc et al., 2012), as well as an incredible morphological diversity, with certain shape facilitating the formation of rapidly sinking aggregates (Alldredge and Gotschalk, 1989; Alldredge and Jackson, 1995; Jackson et al., 2005; Burd and Jackson, 2009; Assmy et al., 2013). Cellular Si:C quota, a key parameter controlling frustule density and sinking rate, varies widely among diatom species (Durkin et al., 2012), in addition of being influenced by environmental parameters such as iron availability (Hutchins and Bruland, 1998; Takeda, 1998). Indeed, numerous iron-fertilization experiments observed higher Si:C and Si:N ratios in diatoms growing under iron-stress, which seemed to indicate the development of more heavily silicified frustules, although it has also been linked to a reduction in cellular organic matter contents (Takeda, 1998; Twining et al., 2004; Hoffmann et al., 2007; Marchetti and Cassar, 2009; Baines et al., 2011). Within a given species, life stages such as auxospores and resting forms can undergo considerable morphological and physiological changes compared to vegetative stages, e.g. heavily silicified resting spores are resistant to grazing (Kuwata and Tsuda, 2005) and can contain up to 10 times more carbon (Doucette and Frixen, 1983; Kuwata et al., 1993), which make them efficient vector to C export (Salter et al., 2012; Rembauville et al., 2015b). At the end, mortality pathways (apoptosis, viral lysis, parasite infection, grazing etc.) will further influence export modes and their efficiency (Kagami et al., 2007; Sherr and Sherr, 2007; Durkin et al., 2016; Kranzler et al., 2019). Despite this apparent complexity, the link between species diversity and particles export is often overlooked. To date, two studies attempted to further refine the diatom functional group into two subgroups occupying different niches in the water column: C-sinker/Group 1 comprise small, fast-growing lightly silicified and colony-forming diatoms that dominate iron-fertilized areas, while Si-sinker/Group 2 are large, slow growing heavily silicified species that thrive in iron-limited areas (Assmy et al., 2013; Quéguiner, 2013).

The Kerguelen region is a good place to study the ecological processes at play in the biological pump, since the area is characterized by contrasted ecosystems differently impacted by iron. Due to its shallow bathymetry (< 700 m) and its great meridional extension, the Kerguelen Plateau acts as a natural barrier diverting both the trajectories of the Antarctic Circumpolar Current (ACC) and the Polar Front (PF) (Park et al., 2008b; Park et al., 2014). Interactions between water masses and the plateau leads to the upward transfer

of iron via diapycnal mixing enhanced by internal wave activity (Blain et al., 2007; Park et al., 2008a), giving an annually recurrent phytoplankton bloom from October to February (Mongin et al., 2008). Past oceanographic surveys investigated the decline and the onset of the diatom bloom (KEOPS1 and KEOPS2 cruises, respectively), by describing diatom community composition (Armand et al., 2008b; Lasbleiz et al., 2016), biogeochemical environments (Lasbleiz et al., 2014), silica production (Mosseri et al., 2008; Closset et al., 2014) and associated carbon export (Savoye et al., 2008; Planchon et al., 2015; Rembauville et al., 2015a).

In this context, the MOBYDICK cruise (Marine Ecosystem Biodiversity and Dynamics of Carbon around Kerguelen: an integrated view) took place in February and March 2018, i.e. at the very end of summer to witness the demise of the diatom bloom, an event that is much less described than the spring bloom, but that nonetheless plays a crucial role in the carbon biological pump. Main objectives of MOBYDICK were 1) to track carbon from its initial fixation at the surface to its channeling through the food web or export into the deep ocean; and 2) provide a detailed description of the diversity at each trophic level, from microbes to micronekton. In this study, we aim at describing diatom diversity and the composition of the bulk particulate matter, on and off the plateau. In particular, we focused our effort on providing a comprehensive description of diatom community structures, in terms of abundances, carbon biomass, physiological states, and silicification activity at multiple scales, i.e. from the community level to single-cell level. The following questions are addressed: How does iron influence diatom community structure during the demise of the Kerguelen bloom? How do diatoms influence the elemental composition and stoichiometry of the particulate matter? What are the ecological vectors driving Si and C export?

2 Methods

2.1 Sampling strategy

The MOBYDICK cruise was conducted south of the Kerguelen Islands in the Indian sector of the Southern Ocean (SO), aboard the French R/V *Marion Dufresne II* in late austral summer (18 February-27 March 2018). In this study, coinciding with the demise of the diatom bloom, a total of four stations were investigated with repeated visits at some of them (Figure 1,

Table 1). Two reference stations, M2 (sampled thrice) and M4 (sampled twice), were respectively defined for the Fe-enriched plateau and the HNLC off-plateau area. Two intermediate stations, M1 and M3 were additionally sampled, once and twice respectively. Bottom depths spanned from 520 m at M2 to 4 730 m at M4 (Table 1). According to Pauthenet et al. (2018), station M3 was located within the Polar Frontal Zone (PFZ), whereas the other stations were located in the Antarctic zone (AAZ), with M1 and M4 both situated very close to the PF (Figure 1).

2.2 Hydrology

Seawater collection and vertical profiles of water column properties were made from an array of 24 bottles (12 L) mounted on a rosette equipped with a Seabird SBE-911 plus CTD unit, which also included a fluorometer for detection of chlorophyll *a* (Chl *a*), and a PAR (photosynthetically available radiation) sensor (LI-COR instrument). The mixed layer depth (MLD) was defined as the depth where the potential density equaled the potential density at 10 m + 0.03 kg m⁻³ (de Boyer Montégut et al., 2004). The depth of the euphotic zone (Z_e) was defined as the depth where 1 % of the surface irradiance remained. Discrete water samples were collected at 11 depths down to 500 m at the plateau station M2 and down to 1000 m at the other stations.

2.3 Inorganic nutrients

Samples were collected in 125 mL HDPE bottles directly from the Niskin bottles. The samples were then filtered on 0.45 µm cellulose acetate filter and preserved with 100 µL HgCl₂ (4g L⁻¹) in 20 mL vials, which were then stored in the dark at room temperature until analysis in the laboratory. For NO₃⁻, PO₄³⁻, and H₄SiO₄, the preserved samples were analyzed in the laboratory with a segmented flow analyzer (Skalar) equipped with colorimetric detection using the classical methods described in Aminot and Kérouel (2007). The accuracy of the methods was assessed using reference material (Certipur, Merck). The precisions were in the range of 1-4 %, and the limit of detection was 0.02 µM for NO₃⁻, 0.03 µM for PO₄³⁻ and 0.05 µM for H₄SiO₄ (Blain et al., 2015).

2.4 Pigments

For pigment measurements, 2.32 L water samples were filtered onto Whatman GF/F filters and stored in liquid nitrogen until analysis. Back at the laboratory, filters were extracted in

100 % methanol, disrupted by sonication, and clarified by filtration (GF/F Whatman) after 2 h. Samples were analyzed within 24 h using High Performance Liquid Chromatography on an Agilent Technologies HPLC 1200 system quipped with a diode array detector following Ras et al. (2008).

2.5 Particulate organic carbon (POC) and nitrogen (PON)

From the rosette sampling, 4 L of seawater were filtered onto precalcinated (450°C, 24h) 25 mm Whatman GF/F filters. Filters were then dried in an oven (40°C, 24h) and stored in a glass vial until analysis. After fumigation with pure HCl (10 h) to dissolve remaining inorganic carbon, analysis of C and N was made with a CHN elemental analyzer calibrated with acetanilide (Rembauville et al., 2016).

2.6 Biogenic silica stock (BSi)

Between 1.5 and 2 L Niskin samples were filtered through 0.4 µm Nucleopore polycarbonate filters. Filters were then rinsed with 0.2 µm filtered seawater, folded in quarters, placed in Petri dishes and dried overnight at 60°C. Filters were kept at room temperature until analyses at the laboratory. The extraction of silicon from biogenic particle phase was performed following the Ragueneau et al. (2005) triple NaOH/HF extraction procedure.

2.7 Plankton counting

Prior to counting, plankton diversity was investigated in few representative samples using a Phenom Pro scanning electron microscope (SEM) in order to resolve the taxonomic list of species at the best possible level for the study area. For SEM analysis, water samples were filtered (50 mL) onto polycarbonate filters (0.8 µm pore size, Whatman), and stored in Millipore Petri Slides at room temperature with no further treatments. Pictures were taken at magnification up to x 25,000.

For plankton counting, seawater samples collected from the same casts and bottles as particulate Si samples were preserved in 250 mL amber glass bottles with 1.6 mL acidified Lugol solution before being stored in the dark at 4°C until analysis. For each station and visit, 8 samples from the surface down to 250 m were counted, giving a total number of 64 samples analyzed. Counting was performed at the laboratory following Utermöhl (1931) using a Nikon TE-200 inverted microscope at magnification X 200. Counted volume varied

between 50 and 100 mL depending on cell concentration. Every planktonic cell examined was counted and identified at the lowest possible taxonomic level. For diatoms, we counted separately cells that were intact (e.g. complete frustule with chloroplasts), empty (e.g. complete frustule devoid of internal content), broken (e.g. frustule with a clean break at the girdle band junction or partly dissolved), or crunched (e.g. frustule with a jagged break outside of the girdle junction; see supplementary Figure S1 for illustrating pictures), as recommended by Assmy et al. (2013). Many mortality pathways can explain the presence of empty and broken frustules (Tréguer et al., 2018), whereas crunched frustules are likely due to handling by copepod mandibles (Assmy et al., 2007). Due to the low magnification, taxonomic identification to the species level was occasionally difficult and necessitated categorizing diatom species to the genus or taxa groupings in the following manner: *Chaetoceros* spp. *Hyalochaete* resting spores (CRS) were not differentiated into species or morphotypes but were counted separately from the vegetative cells; *Fragilariopsis separanda* and *Fragilariopsis rhombica* were grouped as *Fragilariopsis separanda/rhombica*; most of the small (< 10 µm) and intermediate (10–50 µm) unidentified centric diatoms were grouped as *Actinocyclus* spp./*Thalassiosira* spp., after we identified these two genera as the dominant ones, based on SEM images. For some taxa exhibiting a wide range of sizes, size classes were defined to better estimate their carbon biomass. Finally, for a few species, we also distinguished different morphological forms and life stages (Figure S2). In *Odontella weissflogii*, we counted separately vegetative cells (rectangular, lightly silicified, with 4 processes located on each valve), resting cells (more rounded and silicified, with two processes on each valve), and resting spores (oval shape, heavily silicified, with very short processes) (Hoban et al., 1980). In *Eucampia antarctica*, many different morphological forms were observed: a typical form (i.e. heavily silicified, asymmetric cells that form coiling chains), a H-shape form, a flat form without horns, and some intermediate forms. Finally, three forms of *Chaetoceros atlanticus* were distinguished: a colonial form with cells having long and straight setae, a single cell form with sigmoidal thickened setae, and a 'bulbosum' form characterized by a single cell enriched with lipids and with short and inflated setae. Although non-exhaustive, a detailed list of taxa is presented in supplementary Table S1, along with linear measurements used to estimate biovolumes and carbon biomasses.

2.8 Estimation of the diatom C biomass

Specific C biomass was assessed only for diatoms, following the methodology described in Cornet-Barthaux et al. (2007). When possible, cell dimensions were determined from at least 20 representative cells for each species/taxon and for each sample. When the third dimension was not measurable due to the cell's position on the slide (e.g. the transapical axis of *Fragilariopsis* species, or the pervalvar axis of numerous centric), the hidden dimension (*hd*) was estimated by using mean dimension ratios from other comparable samples where *hd* was measured. For a few taxa (e.g. centrics such as *Asteromphalus* spp.), *hd* was not measured in any sample. In these cases, we used the visible to hidden dimension ratio documented for the same genera in European standards (Afnor, 2015). For each measured cell, a biovolume was estimated using linear dimensions in the appropriate geometric formula reflecting the cell shape (Afnor 2015). A mean biovolume was then estimated for each taxon and converted to carbon content per cell according to the corrected equation of Eppley (Smayda, 1978) as follows:

$$\text{Log}_{10} \text{ C biomass (pg)} = 0.75 \text{ Log}_{10} (\text{cell volume } (\mu\text{m}^3)) - 0.352$$

CRS carbon content was estimated using the volume-to-carbon relationship of 0.039 pmol C μm^{-3} established from the resting spore of *Chaetoceros pseudocurvisetus* (Kuwata et al., 1993). C content per cell (pg cell⁻¹) was multiplied by cell abundance (cells L⁻¹) to derive total carbon biomass per taxon, expressed in units of $\mu\text{g C L}^{-1}$. Total diatom carbon biomass was then compared to chemically determined POC concentrations to yield a percentage contribution of diatoms to the total POC fraction.

2.9 Diatom-specific contribution to silica deposition

Taxon-specific silica production was quantified using the fluorescent dye PDMPO. Leblanc and Hutchins (2005) have shown that the dye is incorporated in a nearly constant ratio with biogenic silica during the synthesis of the frustule, allowing semi-quantification of newly deposited Si at the specific level using epifluorescence microscopy. However, McNair et al. (2015) observed a linear decrease in the BSi : PDMPO incorporation ratio when ambient silicic acid concentration fall below 3 $\mu\text{mol L}^{-1}$. Hence, it is important to keep in mind that for a given PDMPO fluorescence, the amount of BSi synthesized might be higher at stations where Si(OH)_4 reached 3 $\mu\text{mol L}^{-1}$. For each station/visit, seawater samples were collected at 5 different depths corresponding to different levels of PAR (50%, 25%, 4%, 1% and 0% of

surface irradiance). For each sample, 150 mL of seawater were spiked onboard with 0.125 μM PDMPO (final concentration). Samples were then placed in deck incubators cooled by running sea surface water and fitted with blue plastic optical filters to simulate the light attenuation of the corresponding depth. After 24 h, samples were filtered onto 0.6 μm black Nucleopore polycarbonate filters. Filters were directly mounted onto permanent glass slides and stored in the dark at -20°C until analysis. Back at the laboratory, microscope slides were observed under a Zeiss Axio Observer Z1 inverted fluorescence microscope equipped with an Xcite 120LED source and a CDD black and white AxioCam-506 Mono (6 megapixel) camera fitted with a filter cube (Ex: 350/50; BS 400 LP; Em: 535/50). For each taxon, fluorescent cells were identified and counted, and we differentiated between valves and girdle bands, since those two parts of the frustule do not mature at the same stage during the cell cycle, and also do not have the same area nor degree of silicification (i.e. the amount of BSi deposited per unit surface), and should thus not be compared directly. In each sample, a representative number of images was taken for each taxon (at least 20 images for the most common taxa). PDMPO fluorescence intensity was then quantified using a custom-made IMAGE J routine on original TIFF images. This routine needs to be changed depending on the format of images and associated information and can be made available upon request to the corresponding author. The taxon-specific contributions to silica production were estimated by multiplying the number of fluorescent cells by the mean fluorescence per cell. The total fluorescence per taxon was expressed in AU (arbitrary unit) L^{-1} . Based on the images we also estimated the degree of silicification for the most active taxa by dividing individual cell fluorescence by its corresponding frustule surface.

2.10 Statistical analysis

Multivariate analyses were performed on total diatom abundances (i.e. including both intact and detrital cell counts) using MATLAB, version 8.4 (MathWorks). The abundances were $\text{Log}(x+1)$ transformed to decrease the importance of numerically dominant taxa. Bray-Curtis dissimilarities were then calculated between each pair of samples, and a cluster analysis was run using the complete linkage algorithm (Legendre and Legendre, 2012). An arbitrary threshold was applied to separate samples into compact clusters. A non-metric multidimensional scaling (NMDS) was also performed on total diatom abundances. The NMDS displays the relative similarity between samples as the distance between points in a

two-dimensional space. Hence, tightly grouped samples are more similar than widespread data points, thereby providing a visual representation of community differences. A comprehensive list of the taxa included in these two analyses is presented in supplementary Table S2.

3 Results

3.1 Hydrographic context

The mixed layer depth (MLD) at the first visit did not exhibit large variations between stations, ranging between 63-79 m (Table 1). M1 was weakly stratified and exhibited the shallowest MLD. Following a large storm event (10 March), the MLD deepened slightly at M2-3 (80 m), and more importantly at M3-3 and M4-2 (both at 96 m). The depth of the euphotic zone (Ze) was shallower above the plateau reference station (58-64 m) compared to the other stations (89-105 m).

Average vertical profiles of Chl *a* concentrations calculated from several visits at a same station are presented in Figure 2.a. Phytoplankton biomass was low at the 4 stations and mostly distributed in the upper 125 m, with the highest concentrations (up to $0.4 \pm 0.2 \mu\text{g L}^{-1}$) reached at the plateau reference station M2. Station M3 and M4, located on the western side of the Kerguelen Plateau, presented the lowest Chl *a* concentrations ($< 0.2 \mu\text{g L}^{-1}$) whereas M1 presented intermediate concentrations ($0.3\text{-}0.4 \mu\text{g L}^{-1}$) in the upper 75 m. The third visit at M2 was marked by an increase in Chl *a* (up to $0.6 \mu\text{g L}^{-1}$ at 50 m, data not shown) following the storm event, explaining the larger standard deviation at this site.

Average profiles of silicic acid, nitrate, phosphate, and ammonium concentrations are presented in Figure 2.b-e. Silicic acid concentrations were depleted in the upper 75 m, especially at station M2 and M3, ranging between $1.7\text{-}3.1 \mu\text{mol L}^{-1}$. In comparison, moderate to elevated silicic acid concentrations were observed at M4 (up to $4.8 \mu\text{mol L}^{-1}$ within the upper 75 m) and M1 (up to $6.9 \mu\text{mol L}^{-1}$ within the upper 50 m). Nitrate and phosphate concentrations were replete in the upper 75 m and ranged between $21.5\text{-}25.1 \mu\text{mol L}^{-1}$ and $1.5\text{-}1.9 \mu\text{mol L}^{-1}$, respectively. Small differences were observed between stations and visits, as evidenced by the low standard deviations. Maximum NH_4^+

concentrations ranged between 0.9-1.3 $\mu\text{mol L}^{-1}$ for the 4 stations, and were usually located in sub-surface.

3.2 Elemental composition (Si, N, C) and stoichiometry of particulate matter

3.2.1 Vertical distribution of particulate matter

BSi, POC, and PON vertical distributions are presented in Figure 3. Stations M2, M3, and M4 were characterized by a marked deep silica maximum (DSM) at the first visit that progressively diminished throughout the survey, whereas no DSM was observed at M1. At M2, the DSM was located at 100 m where BSi reached 1.7 $\mu\text{mol L}^{-1}$ at the first visit, decreasing to 0.7 $\mu\text{mol L}^{-1}$ at the last visit (18 days later), while an increasing trend was observed in the upper 75 m. At M3, BSi concentrations reached 2.0 $\mu\text{mol L}^{-1}$ at the DSM located at 125 m, which deepened down to 150-175 m at the next visit (15 days later). The highest siliceous biomass was measured at station M4, located upstream of the Fe-fertilized plateau, where BSi reached 3.2 $\mu\text{mol L}^{-1}$ at the DSM (75 m) during the first visit. At M1, Si biomass decreased regularly with depth and never exceeded 1.0 $\mu\text{mol L}^{-1}$. Throughout the study area, BSi concentrations were still elevated down to 350-500 m, varying between 0.3 and 0.8 $\mu\text{mol L}^{-1}$, with the highest values measured at M2.

POC and PON vertical distribution differed from BSi, with a decreasing trend with depth. Highest concentrations were measured at M2-3, where POC and PON concentrations reached 6.2 and 1.0 $\mu\text{mol L}^{-1}$ at 28 m, respectively. This station was also characterized by a large increase in POC and PON concentrations at 450 m, likely reflecting an organic material resuspension event after the storm. Apart from M2-3, no large differences were observed at the surface, with POC and PON varying respectively between 3.3-5.5 $\mu\text{mol L}^{-1}$ and 0.6-0.9 $\mu\text{mol L}^{-1}$, while at the last sampled depths they varied between 0.5-1.9 and 0.1-0.2.

3.2.2 Depth-integrated standing stocks

BSi, POC, PON, and Chl *a* concentrations were integrated between 0 and 200 m (Figure 4; see supplementary Figure S3 for integrated concentrations between 200-500 m), independently of the mixed-layer depth because significant biogenic and organic particulate material was measured between 100 and 200 m (Figure 3). Integrated BSi ranged between

134-219 mmol m⁻² at M1/M2/M3, and a decreasing trend was observed during the survey. In line with vertical profiles, BSi standing stocks were larger at M4 (up to more than twice) where it reached 493 mmol m⁻² at the first visit, decreasing to 339 mmol m⁻² at the second visit. POC and PON standing stocks ranged between 448-756 mmol m⁻² and 73-108 mmol m⁻² respectively, with maximum values measured at M2-1 and lowest values measured at M3-3. Contrary to BSi, no large variations were observed between stations. A decreasing trend was observed between the first and the second visit at M2/M3/M4, but integrated stocks increased after the storm event at the plateau reference station M2 (3rd visit). Chl *a* standing stocks did not vary a lot spatially, especially between M1/M3/M4 where it ranged between 20-33 mg m⁻². Above the plateau, it varied between 30-53 mg m⁻², with the largest increase observed during the last visit, after the storm event.

3.2.3 Stoichiometry of particulate matter

The elemental ratios within the upper mixed layer (0-MLD) and the subsurface layer (MLD-200 m) are presented for the 8 visits at the 4 stations (Figure 5) to highlight some spatial and/or temporal patterns over the study area. Within the ML, the most striking feature was the elevated Si:C and Si:N ratios at M4 (both visits), with average values ranging between 0.54-0.67 and 3.42-4.05, respectively. At the other stations, Si:C (0.14-0.20) and Si:N (0.78-1.16) ratios were much closer to the empirical 0.13 and 1.12 values reported by Brzezinski (1985) for diatoms grown in nutrient-replete medium. Below the MLD, Si:C and Si:N ratios increased rapidly at every station with average values ranging respectively between 0.35-1.06 and 2.13-6.58, with M2-1 still displaying the highest ratios. The average C:N ratios were close to the 6.62 Redfield empirical value. In contrast to Si:C and Si:N, no large variations were observed between the 0-MLD (average: 5.71-6.32) and MLD-200 m layers (6.02-8.38).

3.3 Diatom community structures: abundances, carbon biomasses, and silica deposition activity

3.3.1 Diatom contribution to particulate organic carbon (POC)

Absolute diatom carbon biomass and its relative contribution to POC are presented in Figure 6. Above the plateau (M2), diatom carbon biomass increased progressively between the first and last visits, on average from $10.2 \pm 3.1 \mu\text{g C L}^{-1}$ ($17 \pm 6 \%$ of POC; $n=4$) to $30.7 \pm 2.4 \mu\text{g C}$

L^{-1} (43 ± 6 % of POC) within the upper 75 m. The highest diatom C biomass measured throughout the survey was reached during the last visit at M2 ($34.1 \mu g C L^{-1}$; 69 m), representing 52 % of POC biomass. At the first visit, diatom C biomass was homogeneous down to 100 m due to the accumulation of large *Eucampia antarctica* cells at this depth, while during the two following visits, it decreased rapidly below the MLD, where on average only $3.5 \mu g C L^{-1}$ (16 % POC) and $2.0 \mu g C L^{-1}$ (10 % POC) remained, respectively. It is interesting to notice the low but quasi constant diatom carbon biomass within the 100-200 m layer at the last two visits, which contrasts with the other stations. At the off-plateau station M4, diatom C biomass was stable within the upper 100 m at the two visits, averaging $10.5 \pm 1.8 \mu g C L^{-1}$ (24 ± 6 % of POC; $n=8$). Lowest C biomass were measured at M3, where it averaged $2.1 \pm 0.6 \mu g C L^{-1}$ (6 ± 2 % POC; $n=8$) at the two visits. These low biomasses can be explained by both lower abundances and the presence of diatoms having small biovolumes. In particular, the genus *Fragilariopsis* spp. was mostly composed of small *F. pseudonana* $< 10 \mu m$ at M3, whereas we counted numerous large *F. kerguelensis* at M1 and M4. Finally, diatom C biomass at M1 was homogeneous in the upper mixed layer ($9.6 \pm 0.3 \mu g C L^{-1}$; 16 ± 1 % of POC), then decreased progressively with depth towards quasi non detectable values below 100 m.

3.3.2 Absolute diatom abundances

The vertical profiles of diatom abundances with the contribution of full, empty, broken, and crunched frustules are presented in Figure 7. Overall, total diatom abundances peaked at 50 m and then decreased progressively with depth, except at station M2 where higher abundances were observed below the MLD, and at M3-3 where abundances were homogeneous in the 50-200 m layer. In the upper 75-100 m, abundances were higher at stations M1 and M4, ranging between 9.9 to 16.8×10^4 cells L^{-1} , with the highest number of cells reached at M4-2 (50 m). In contrast, lower abundances were measured at M2 in the upper 75 m, although we observed a progressive increase between the first and last visit, from $3.2 \pm 0.9 \times 10^4$ cells L^{-1} ($n=4$) to $5.8 \pm 0.3 \times 10^4$ cells L^{-1} . The contribution of intact cells to total diatom abundances decreased rapidly below 75 m at M1/M2, whereas it declined significantly only below 100 m at M3/M4 (see also Figure S4). Over the study area, it was homogeneous in the surface layer, with an average contribution of 66 ± 8 % ($n=31$). Above the plateau, numerous intact cells were still observed in the deepest samples located

between 175–200 m (up to 48 % at M2-2), while only 3–12 % of diatoms were still intact at the other stations. The average percentage of empty and broken cells increased with depth from respectively 24 ± 5 % and 3 ± 2 % at the surface ($n = 8$) to 55 ± 9 % and 19 ± 9 % in the deepest samples. The percentage of crunched diatoms, which we consider as indicative of mesozooplankton grazing, did not exhibit either any obvious vertical or spatial trends (5 ± 3 %; $n=64$).

3.3.3 Taxon-specific contribution to total diatom abundances

Both a cluster analysis and a non-metric multidimensional scaling analysis (Figure 8.a and b) performed on total abundances at all sites and depths revealed a strong vertical and spatial structure of diatom communities. The first clustering factor is based on depth, clearly separating samples collected between 0 and 75/100 m (depending on the station) from samples collected below, between 100/125 and 250 m. Secondly, within surface samples, M2 is isolated from the other three stations which cluster together, while at depth two different clusters (M1/M2 vs M3/M4) are identified. The stress value of the NMDS (0.11) indicates a fair model-data fit. The NMDS plot confirms that the four clusters are different from each other in terms of their taxonomic composition, with the first axis separating diatom communities according to their depth, while the second axis highlights the spatial heterogeneity.

Taxon-specific contribution to total diatom abundances is presented in Figure 8.c. In the upper 75 m, diatom community structure above the plateau reference station M2 was clearly distinct from that observed at the other sites. At the first visit, diatoms were dominated by *Actinocyclus/Thalassiosira* spp. (29 ± 3 %; $n=4$), *Thalassionema nitzschioides* (17 ± 3 %), *Guinardia cylindrus* (13 ± 1 %), *Corethron* spp. (only *C. inerme*; 12 ± 1 %), and *Cylindrotheca closterium* (7 ± 4 %). A temporal evolution was observed at this station, with the third visit marked by the increasing contribution of *C. inerme* (27 ± 3 %), *T. nitzschioides* (28 ± 5 %) and *Cylindrotheca closterium* (15 ± 3 %), while *Actinocyclus/Thalassiosira* spp. and *G. cylindrus* decreased. As shown by the cluster analysis, diatom communities in the upper 75–100 m layer were similar between M1/M3/M4 and were dominated by a mix of *Cylindrotheca closterium* (23 ± 14 %), *Actinocyclus/Thalassiosira* spp. (20 ± 5 %), and *Fragilariopsis kerguelensis* (16 ± 10 %). Below the MLD, the diatom community at M2-1 was

characterized by the presence of large and heavily silicified cells of *Eucampia antarctica* (13 ± 6 %; $n=4$) which almost disappeared at the following visits. Excluding this species, deep diatom communities at M2/M1 were similar and dominated by a mix of CRS (27 ± 10 %; $n=17$), *Pseudo-nitzschia* spp. (15 ± 9 %), *Fragilariopsis kerguelensis* (13 ± 5 %), *Chaetoceros* spp. (13 ± 7 %; mostly as small *Chaetoceros* sp. *Hyalochaete*), and *Actinocyclus/Thalassiosira* spp. (10 ± 5 %). Deep communities at stations M3/M4 formed a distinct cluster and were dominated by a mix of *Fragilariopsis kerguelensis* (37 ± 9 %; $n=16$), *Chaetoceros atlanticus* (23 ± 13 %), *Pseudo-nitzschia* spp. (13 ± 5 %), and *Actinocyclus/Thalassiosira* spp. (11 ± 3 %), while the contribution of CRS was minor at these sites.

When looking at the taxon-specific contribution to intact and detrital cells (see supplementary Figure S5-8), some trends emerged. The only species that was almost exclusively observed intact at all sites within the mixed layer was *Cylindrotheca closterium* reflecting its possible recent growth and good physiological state at the time of sampling. Below the MLD, *Chaetoceros atlanticus* and the other *Chaetoceros* species (including both vegetative and resting stages) were the main contributors to intact cells, at M3/M4 and M2/M1 respectively, while *Fragilariopsis kerguelensis* cells were mostly detrital (i.e. empty, broken or crunched). Crunched frustules were mainly associated with the pennate *Fragilariopsis kerguelensis* (42 ± 21 %; $n=64$) and the centric genera *Actinocyclus/Thalassiosira* spp. (24 ± 15 %), suggesting a selective grazing.

3.3.4 Taxon-specific contribution to diatom carbon biomass

Taxon-specific contribution to diatom carbon biomass is presented in Figure 9. At the reference plateau station M2, diatom carbon biomass was dominated within the upper 75 m (i.e. corresponding to the MLD) by the large centric species *Corethron inerme*, whose average contribution to biomass increased from 59 ± 3 % (1st visit, $n=4$) to 83 ± 5 % (3rd visit). Important contributors were also *Guinardia cylindrus* at the first visit (19 ± 5 %; $n=4$), followed by species belonging to *Proboscia/Rhizosolenia* genera (mostly *P. alata* and *R. chunii*) whose contribution was 10 ± 4 % ($n=12$) at the three visits. The taxa *Actinocyclus/Thalassiosira* spp., *Thalassionema nitzschioides*, *Pseudo-nitzschia* spp., and *Cylindrotheca closterium* which were key contributors to diatom abundances did not contribute significantly to C biomass, due to their low biovolumes. Below the MLD, C

biomass was largely dominated by *Eucampia antarctica* at the first visit (58 ± 11 %; $n=4$). Its contribution rapidly decreased at the following visits (11 ± 9 %; 3rd visit), being replaced by CRS (27 ± 18 %) and *Chaetoceros* spp. (23 ± 17 %; mostly the small *Chaetoceros* sp. *Hyalochaete*). Apart from M2, the community structures at the other stations appeared more diverse. The large centric species *Proboscia/Rhizosolenia* spp. contributed significantly to carbon biomass throughout the water column, except below 100 m at M1 (mostly *P. inerme* and *R. chunii*; 18 ± 11 %, $n=35$). Species belonging to *Actinocyclus/Thalassiosira* genera were also important contributors all over the water column (21 ± 10 %; $n=40$). Although a vertical structure was less obvious compared with diatom abundances (Figure 8), *Chaetoceros atlanticus* contributed significantly to C biomass below the MLD at M3/M4 (26 ± 15 %; $n=18$), while *Chaetoceros* spp. (mostly the small *Chaetoceros* sp. *Hyalochaete*; 22 ± 12 %; $n=5$) and CRS (22 ± 13 %) were the main contributors at M1 below 100 m. Interestingly, one can notice the much lower contribution of *Fragilariopsis kerguelensis* to C biomass in comparison with diatom abundances, which can be linked to its high percentage of detrital frustules, especially below the mixed layer, as well as to their small C content per cell (149 pg C cell⁻¹; see supplemental Table S1). Although it had one of the smallest biomasses ($8-25$ pg C cell⁻¹), *Cylindrotheca closterium* contributed on average to 17 ± 11 % of diatom C ($n=8$) in the upper 100 m at M3, due to elevated abundances. *Corethron* spp. contributed significantly to C biomass at some depths at station M1/M3/M4, but unlike M2, it belonged mainly to the species *C. pennatum*.

3.3.5 Taxon-specific contribution to biogenic silica deposition

The contribution of each taxon to biogenic silica deposition is presented in Figure 10. The diversity appears smaller than in the previous figures for several reasons: first, species identification is harder in epifluorescence than in bright-field microscopy and leads to downgrading of the upper taxonomic level; second, because less species were actively silicifying in a given sample relative to the total number of taxa, meaning that some species were not active at the time of the incubation even though present as intact cells.

Above the plateau station M2, total PDMPO fluorescence increased progressively between the first and the last visit from a maximum of 4.1×10^6 AU L⁻¹ (M2-1; 19 m) to 12.1×10^6 AU L⁻¹ (M2-3; 9 m). This increasing silicification activity was associated with the development of

Corethron inerme whose average contribution to total silicification was low at M2-1 (13 ± 10 %; $n = 3$), but increased to 52 ± 9 % ($n = 4$) and 47 ± 6 % ($n = 4$) at M2-2 and M2-3, respectively. *Proboscia/Rhizosolenia* spp. (mostly *P. alata*) were also actively silicifying, with an average contribution of 39 ± 16 % ($n = 11$) to PDMPO fluorescence throughout the survey. *Fragilariopsis* spp. cells (likely including *F. kerguelensis*, although identification to the species level was difficult) were actively silicifying at this station, albeit as a smaller contributor (14 ± 10 %; $n = 11$). At M2, we also incubated samples that were collected at 100 and 125 m (data not shown), but silicification activity was almost null, and we did not observe any labelled *Eucampia antarctica* or CRS, although they were important contributors to both abundances and C biomass at those depths. The lowest total PDMPO fluorescence was measured at M3-1 ($< 1.0 \times 10^6$ AU L⁻¹) where silicification activity was almost constant throughout the upper 100 m. Very few taxa contributed to biogenic silica deposition, which was dominated by the activity of *Fragilariopsis* spp. (48 ± 17 %; $n = 4$) and *Actinocyclus/Thalassiosira* spp. centric cells (44 ± 15 %; $n = 4$). By contrast, the highest total PDMPO fluorescence was measured at M1, reaching 25.0×10^6 AU L⁻¹ at the surface before decreasing progressively with depth. At this station, *Fragilariopsis* spp. and *Actinocyclus/Thalassiosira* spp. were the most important contributors down to 90 m (respectively 31 ± 18 %, and 30 ± 19 %; $n = 4$). Actively silicifying *Corethron pennatum* were also observed at the surface (47 % at 13 m), whereas *Rhizosolenia* spp. and *Chaetoceros* spp. were observed deeper, contributing respectively to 21 % at 60 m and 10 % at 90 m. At the reference HNLC station M4, total PDMPO fluorescence was close to M1, reaching 21.0×10^6 AU L⁻¹ at M4-1 (29 m). This station was also the most diverse in terms of silicifying community. Indeed, throughout the two visits ($n = 8$), many different taxa were producing new frustules, including *Fragilariopsis* spp. (30 ± 12 %), *Actinocyclus/Thalassiosira* spp. (21 ± 10 %), *Proboscia/Rhizosolenia* spp. (16 ± 13 %), *Corethron pennatum* (9 ± 11 %), *Chaetoceros dictyota* (5 ± 5 %), *C. atlanticus* (4 ± 4 %), and *Membraneis* spp. (4 ± 6 %). Based on McNair et al. (2015) experimental results, which showed that the BSi : PDMPO incorporation ratio was higher at $[\text{Si}(\text{OH})_4] > 3 \mu\text{mol L}^{-1}$, it is plausible that relative differences between M1/M4 ($[\text{Si}(\text{OH})_4] > 3 \mu\text{mol L}^{-1}$ within the mixed layer) and M2/M3 ($[\text{Si}(\text{OH})_4] < 3 \mu\text{mol L}^{-1}$) in terms of total PDMPO fluorescence would be even higher if converted to new BSi.

3.4 Species-specific properties driving diatom elemental stoichiometry

3.4.1 Diatom Si:C ratio

Si:C ratios based on calculated diatom carbon biomass (defined hereafter as Si:C_{diatom}) instead of total POC are presented in Figure 11. Within the ML, Si:C_{diatom} ratios were well above the 0.13 value reported by Brzezinski (1985) with the highest values measured at M3/M4 (range: 2.4-3.6), intermediate values at M1 (1.2-1.3), and the lowest ones at M2 (range: 0.4-0.9). Above the plateau, a decreasing trend was observed throughout the survey period. Overall, such elevated Si:C_{diatom} ratios in the upper layer can be explained by several factors including the presence of detrital frustules, a high silicification degree, or a low carbon content per cell. Below the ML, Si:C_{diatom} ratios increased drastically with average values between 3.7-20.8, evidencing the preferential recycling of soft organic matter over BSi dissolution. At 200 m, where a significant fraction of diatom organic matter is likely to have been remineralized, Si:C_{diatom} were still much lower at M2 in comparison with stations located outside the plateau.

3.4.2 Diatom silicification degree

The degree of silicification (i.e. the quantity of BSi deposited per surface unit) was semi-quantitatively estimated by normalizing the PDMPO fluorescence of each labelled cell with its labelled surface area (expressed in Arbitrary fluorescence Unit per μm^{-2}). Figure 12 shows the degree of silicification for the most important contributors to BSi deposition. Small ($< 10 \mu\text{m}$) *Actinocyclus/Thalassiosira* spp. were less silicified at the iron-fertilized station M2 during the first two visits (Mann-Whitney U test, $p < 0.05$), whereas no significant differences were observed between the other stations. This was even more evident for the 10–30 μm size fraction characterized by a mean silicification degree equal to $0.51 \pm 0.30 \text{ AU } \mu\text{m}^{-2}$ at M2-1/M2-2, which was 3-4 times lower than at other stations ($1.46\text{-}2.38 \text{ AU } \mu\text{m}^{-2}$) but tended to increase during the successive visits. Diatoms belonging to the genus *Fragilariopsis* (small and large) were the most heavily silicified of all actively silicifying species. However, statistical analysis showed their degree of silicification was significantly lower at M2 (range: $2.44\text{-}2.70 \text{ AU } \mu\text{m}^{-2}$ and $1.40\text{-}2.12 \text{ AU } \mu\text{m}^{-2}$ for the size-classes <10 and 10–30 μm , respectively) in comparison with M1/M4 (range: $3.34\text{-}5.39 \text{ AU } \mu\text{m}^{-2}$ and 3.91-

7.40 AU μm^{-2}). Actively silicifying *Corethron inerme* were mostly observed at station M2 (Figure 10). Girdle bands of *C. inerme* were weakly silicified (mean: 0.70 ± 0.31 AU μm^{-2} ; $n = 133$). Half-valves of *C. inerme* were more silicified with an average silicification degree equal to 2.70 ± 1.19 AU μm^{-2} ($n = 54$). Labelled girdle bands of *Proboscia alata* were also numerous at M2/M4. Again, the degree of silicification was significantly lower at the plateau station M2 for the three visits (1.58 ± 0.46 AU μm^{-2} , $n = 111$) compared with the reference HNLC station M4-1 (2.87 ± 0.85 AU μm^{-2} , $n = 7$). Although not a dominant contributor to BSi deposition, we found that *Chaetoceros atlanticus*, an important contributor to both abundances and carbon biomass at M3/M4, was weakly silicified (1.04 ± 0.78 AU μm^{-2} , $n = 71$).

3.4.3 Diatom species-specific physiological state below the mixed layer

A detrital:intact cell ratio (defined hereafter as D:I ratio) averaged over the deep MLD-250 m layer was calculated to determine the physiological state of the cells exported out of the mixed layer (Table 2). Following Rembauville et al. (2015b), we used the threshold values of 2 (representing species mainly observed as detrital cells) and 0.5 (representing species mainly observed as intact cells). Among the main contributors to total diatom abundances below the ML (Figure 8), diatom taxa displaying D:I ratios > 2 were in decreasing order of importance: *Fragilariopsis kerguelensis*, *Pseudo-nitzschia* spp., *Actinocyclus/Thalassiosira* spp., and *Chaetoceros atlanticus*, indicating those taxa were mostly empty, broken or crunched below the MLD. Instead, *Chaetoceros* spp. (mostly a small *Chaetoceros* sp. *Hyalochaete*) and CRS displayed D:I ratios < 0.5 at M2, meaning they were preferentially found intact below the ML. *Eucampia antarctica* displayed ratios in between the thresholds < 2 and > 0.5 at M2-1 where it was an important contributor to diatom abundances, meaning this species was equally represented by full and empty cells. Finally, some taxon that were numerically important at the surface were few in number below the MLD (e.g. *Fragilariopsis* spp. such as *F. pseudonana*, *Corethron inerme*, *Cylindrotheca closterium*), suggesting they were not efficient vectors for both Si and C export.

4 Discussion

The MOBYDICK results presented above make it possible to draw the major characteristics of the final stage of the seasonal bloom around the Kerguelen Plateau by illustrating the relationships between the structure of its diatom communities and its regional biogeochemistry. While past oceanographic surveys (KEOPS1: January/February 2005; KEOPS2: October/November 2011) identified the physical mechanisms leading to the vertical input of iron-rich deep waters which are responsible for the recurrent plateau bloom development (Blain et al., 2007; Park et al., 2008a), the MOBYDICK project focused on the study of the relationships that exist between the oceanic biodiversity and the operation of the biological carbon pump. In this paper we specifically address the question of the elemental composition and stoichiometry of particulate matter and how these parameters may be driven by diatom community composition and species-specific properties (e.g. physiological state, life stages, carbon content, silicification degree etc.), above the Fe-fertilized plateau and in offshore waters.

4.1 Biogeochemical environments at the final stage of the Kerguelen bloom

At the beginning of our survey (February 26th), the siliceous biomass at station M2 located above the Kerguelen Plateau had mainly accumulated within a deep silica maximum (DSM) located at 100 m ($1.7 \mu\text{mol L}^{-1}$), before progressively receding at the following visits. An opposite trend was observed in the upper 75 m corresponding to the mixed layer (ML), where BSi slightly increased from 0.6 to $0.8 \mu\text{mol L}^{-1}$, while a three-fold diatom C biomass increase (10.2 - $30.7 \mu\text{g C L}^{-1}$), occurred following the development of a population of large *Corethron inerme*. However, these concentrations were fairly low by comparison to diatom biomasses measured earlier in the season both for Si (up to $21.3 \mu\text{mol L}^{-1}$; Mosseri et al., 2008) and C (up to $100 \mu\text{g C L}^{-1}$; Armand et al., 2008b). Contrary to BSi, Chl *a*/POC/PON standing stocks did not show large variations between on- and off-plateau stations, which can be attributed to the decaying stage of the yearly bloom. Silicic acid concentrations were depleted ($1.2 \mu\text{mol L}^{-1}$ at the surface) whereas nitrate and phosphate levels were still elevated, which confirms the high H_4SiO_4 uptake affinity of diatoms previously mentioned by Mosseri et al. (2008) over the Kerguelen Plateau. Inputs of H_4SiO_4 through vertical mixing enhanced by internal waves (Park et al., 2008a), as well as BSi dissolution evidenced by Closset et al. (2014) could have sustained this persisting diatom community. In addition, a

large storm event on March 10th with wind speeds up to 50 knots for two days led to a deepening of the MLD during the last visits at M2/M3/M4 (Table 1), enabling a pulse input of H_4SiO_4 in the surface layer. This input must have been limited and, although diatom growth was stimulated, we observed a rapid emergence of Si limitation signs on the plateau where H_4SiO_4 concentrations and Si:N ratios were at the lowest: (1) SEM images as well as PDMPO single-cell analysis revealed that *Corethron inerme* frustules were very weakly silicified, with collapsed frustules in most images, (2) germination experiments performed on *Odontella weissflogii* resting spores (Leblanc et al., in prep.) incubated under two different treatments (light + Si + P vs. light only) indicated that Si addition was the main factor triggering spore germination.

On the western side of the Kerguelen Plateau, it is unlikely that station M3 and M4 were influenced by iron fertilization from the plateau, due to the eastward flow associated with the PF (Park et al., 2008b; 2014; Zhou et al., 2014). These two stations were marked by an important deepening of the MLD following the storm (from 69 to 96 m) but Ze was always deeper (from 95 to 101 m) suggesting that diatoms were not prone to light limitation in this area. However, stations M3 and M4 exhibited contrasted biogeochemical environments. At M3, silicic acid concentrations were low at the surface ($2.4 \mu\text{mol L}^{-1}$), suggesting a strong H_4SiO_4 limitation since Southern Ocean diatoms have long been shown to exhibit very high K_s values for H_4SiO_4 under HNLC conditions (Jacques, 1983; Nelson and Tréguer, 1992; Franck et al., 2000; Nelson et al., 2001; Quéguiner, 2001; Mosseri et al., 2008). As a matter of evidence, diatom abundances decreased sharply throughout the survey period while silicification activity as well as diatom contribution to C (average in the ML: 5 % POC) were the lowest recorded during the cruise. This station has been extensively studied during past oceanographic surveys (e.g. KEOPS1 & 2) and corresponds to the time series station KERFIX (Jeandel et al., 1998). These studies reported very low diatom productivity year-round in these waters with C biomass rarely exceeding $3 \mu\text{g C L}^{-1}$ (Kopczyńska et al., 1998; Lasbleiz et al., 2016), and phytoplankton abundances largely dominated by naked pico- and nanoflagellates (Kopczyńska et al., 1998). According to Pauthenet et al. (2018), the zonal position of the PF is highly variable throughout the productive season on the westernside of the plateau and is located further south by up to 4° latitude in March compared to September. Hence, it isolates M3 from the southern Antarctic surface water (AASW), giving

one potential explanation to the lower diatom contribution in this area, since flagellates are known to outnumber diatoms north of the PF (Kopczynska et al., 1986). In a study investigating the whole microplankton community structure across the Subantarctic and Polar Front, Rembauville et al. (2016) also showed that dinoflagellates and ciliates dominated microplankton POC in the PFZ, while diatoms dominated in the AAZ. Unexpectedly, we measured the highest siliceous biomass at the reference HNLC station M4, where BSi concentrations reached $3.2 \mu\text{mol L}^{-1}$ at the DSM (1st visit), then started to decrease shortly after. Intermediate silicic acid concentrations were measured ($\approx 4.5 \mu\text{mol L}^{-1}$) that appeared however sufficient for diatoms to grow since they were actively silicifying within the upper 100 m (Figure 10). Elevated BSi concentrations in HNLC waters were also reported in a similar HNLC environment earlier in the season, reaching $6.5 \mu\text{mol L}^{-1}$ at the end of January (Mosseri et al., 2008). Heavily silicified species (e.g. *Fragilariopsis kerguelensis*) were particularly abundant at M4-1, which likely drove BSi towards elevated values. Hence, our results show that diatoms can maintain a significant Si biomass in HNLC waters, even exceeding those measured above the plateau at the end of the productive period.

On the eastern side of the Kerguelen Plateau, M1 was likely not limited by nutrients since we did not observe a DSM characterizing nutrient depleted waters and H_4SiO_4 concentrations were the highest (range: $6.6\text{-}6.2 \mu\text{mol L}^{-1}$) we have recorded. By contrast with M3 and M4, iron could have been supplied to this station by the transport of Fe-rich waters that circulate from the Kerguelen-Heard shelf basin into the deep basin east of the Kerguelen Islands (van Beek et al., 2008; Park et al., 2014). The ML was weakly stratified, which could have promoted nutrient diffusive input from the deep reservoir. Diatoms in this region were the most actively silicifying, yet they did not reach a significant Si biomass ($\text{BSi} < 1 \mu\text{mol L}^{-1}$). Grazing could have prevented biomass accumulation, which is substantiated by elevated concentrations of pheopigments at this station (Irion et al., submitted).

All our observations agree as to the presence of a final phase of the seasonal phytoplankton development on all of the stations studied. However, differences are apparent in the factors controlling the emerging biogeochemical properties. The geographic location in relation to the plateau but also in relation to the PF (via the influence of the AASW) leads us to consider

a modulation of these properties by the degree of limitation by iron and/or H_4SiO_4 and the intensity of grazing, both having direct effects on the structure of phytoplankton communities and their physiological state as will be discussed in the following sections.

4.2 The influence of diatom communities on C:N:Si elemental ratios

Redfield (1958) stated that “the environment not only determines the conditions under which life exists, but the organisms influence the conditions prevailing in their environment”. Later on, Redfield et al. (1963) provided the bases for reflecting upon the influence of the physiology of organisms on the composition of seawater, giving rise to the so-called ‘Redfield-Ketchum-Richards (RKR) ratio’ $\text{C/N/P} = 106/16/1$. Towards the end of the 90’s the emphasis was shifted to the role of the environment on the stoichiometry of particulate organic matter and the influence of iron availability on diatom stoichiometry has been widely recognized and elevated at the paradigm level (Hutchins and Bruland, 1998; Takeda, 1998; Hoffmann et al., 2007; Baines et al., 2010). Following this paradigm, diatoms growing in Fe-depleted HNLC waters should have higher (2-3 times) Si:C and Si:N ratios when compared to some empirical values ($\text{Si:C} = 0.13$, $\text{Si:N} = 1.12$) determined by Brzezinski (1985), which is supposed to indicate the development of more heavily silicified diatoms. Nevertheless, lower Si content relative to C and N under high iron conditions can be linked to either an increase in cellular organic matter or a decrease in cellular BSi concentration, highlighting the species-specific response to iron enrichment (Takeda, 1998; Twining et al., 2004; Hoffmann et al., 2007; Baines et al., 2011). Finally, a few studies pointed out that elemental ratios are primarily driven by taxonomic composition of resident diatom communities rather than a short term physiological response to iron addition (Hoffmann et al., 2006; Baines et al., 2010; Closset et al., 2014; Lasbleiz et al., 2014), again highlighting the primary role played by phytoplankton community structures in driving the biogeochemical cycles.

In our study, mixed layer Si:C and Si:N ratios in the bulk particulate matter (Figure 5) were close to the empirical values of Brzezinski (1985) at M1/M2/M3 (0.11-0.20 and 0.65-1.16, respectively) while they were significantly higher at the HNLC reference station M4 (0.52-0.59 and 3.36-3.66, respectively), which at first sight could indicate the presence of more heavily silicified diatoms. However, care should be taken when drawing conclusions about

the diatom silicification degree based solely on particulate matter ratios. Indeed, these ratios result from the net effect of species-specific Si:C and Si:N composition (Sackett et al., 2014), subsequent species-specific mortality pathways, diatom contribution to particulate organic matter and the presence of detrital particulate Si.

Further insight can be gained by looking at a Si:C_{diatom} ratio (Figure 11) based on calculated diatom carbon biomass rather than the bulk POC measurements, which include both autotrophic and heterotrophic biomass as well as phytodetritus and faecal pellets. Since other organisms bearing siliceous skeleton like rhizarians or silicoflagellates were negligible compared with diatoms in our study, this ratio is more representative of diatom elemental Si:C ratios although it is still subject to overestimation because it includes detrital diatom fragments within BSi (average: 33 ± 7 % of broken/empty/crunched frustules without considering smaller unidentifiable fragments). In the ML, Si:C_{diatom} ratios (> 0.4) were well above the empirical value of 0.13 (Brzezinski, 1995) at all stations. Such elevated ratios in the study area may be driven by the presence of detrital fragments of heavily silicified species (see supplementary Figure S6), such as those coming from *Fragilariopsis* cells at M1/M3/M4 and *Thalassionema nitzschioides* at M2. It is also plausible that Southern Ocean diatoms have Si:C ratios higher than Brzezinski's empirical value, which was obtained from temperate and tropical species cultivated under nutrient-replete conditions. Indeed, recent studies indicate that polar diatoms Si:C ratios could reach values up to 0.87 (Lomas et al., 2019) and Southern Ocean species could be 11-fold more silicified than diatoms cultured in nutrient replete conditions (Baines et al., 2010). This is to be compared with the results of Quéguiner and Brzezinski (2002) who reported Si:C production ratios ranging between 0.54-1.19 at the onset of a diatom bloom in the polar frontal zone of the Atlantic sector. During KEOPS, Mosseri et al. (2008) also measured higher Si:C and Si:NO₃ elemental uptake ratios in HNLC waters in comparison with Fe-fertilized waters, which they suggested was attributable to the development of more heavily silicified diatoms.

The Si:C_{diatom} ratios outside the plateau (average: 1.2-3.6) were much higher than over the plateau (average: 0.4-0.9). Based on PDMPO single-cell analysis (Figure 12), our data suggest that these differences are related to Southern Ocean diatom specificities. Within a given taxon (e.g. *Fragilariopsis* spp., *Actinocyclus/Thalassiosira* spp.), active diatoms were more

heavily silicified outside the plateau at M1/M4, which supports the classical view that iron limitation leads to higher silicification degree and Si:C ratios (Hutchins and Bruland, 1998; Takeda, 1998; Hoffmann et al., 2007; Baines et al., 2010). However, the elevated Si:C_{diatom} ratios at M3 were also most likely driven by community differences, with the presence of smaller diatoms (e.g. *Fragilariopsis pseudonana*) known to be heavily silicified and with low C content due to their small biovolume, a characteristic which would therefore be added to the physiological response to iron stress (Marchetti and Cassar, 2009). Hence, regardless of the effects of iron on diatom physiology, the community composition itself strongly drives community silicification and elemental ratios. Heavily silicified *Fragilariopsis* frustules were numerous outside the plateau, while they were absent within the ML at M2 where we observed many weakly silicified *Corethron inerme* frustules. Discrepancies between elemental ratios in the bulk particulate matter and in diatoms can be attributed to the contribution of non-diatom components to total POC. As an illustration of this, the very low diatom contribution to total POC at M3 tended to attenuate the diatom signal, which resulted in low Si:C and low Si:N ratios in the bulk particulate matter, similar to those measured above the plateau, although diatom elemental ratios were much more elevated at M3.

The combination of our measurements integrating biogeochemical analyses, fine microscopic observations of the state of diatoms, and their silicification activity measured by the PDMPO method then suggest that the higher diatom elemental ratios outside the plateau were likely related to the combined effects of both taxonomic composition and a direct physiological response to iron stress, with key taxa e.g. *Fragilariopsis* spp. driving ratios toward elevated values. The response to iron stress is therefore a complex process integrating both the selection of dominant species which are particularly silicified and an ecophysiological response via the slowing down of their cell cycles.

4.3 Ecological dynamics and the seasonal phytoplankton succession in the Kerguelen area

Our statistical analysis revealed that depth was the main factor shaping diatom community structure, with one community roughly located within the upper mixed layer while a different one was systematically found within the pycnocline discontinuity (Figure 8). Spatial

heterogeneity acted as a second factor separating on- versus off-plateau stations, hence, highlighting the role played by particular biogeochemical environments in structuring diatom communities (Lasbleiz et al., 2014; Lasbleiz et al., 2016).

Above the plateau, the mixed layer community was characterized by the presence of the large centric species *Corethron inerme* and *Guinardia cylindrus* (1st visit only), in association with *Thalassionema nitzschioides*, *Cylindrotheca closterium*, and the centric genera *Actinocyclus/Thalassiosira* spp. Despite depleted H_4SiO_4 concentrations, *C. inerme* was actively growing as evidenced by an increase of its numerical abundance, its silicification activity, and its contribution to diatom C biomass. Interestingly, this species has a small surface to volume ratio (Cornet-Barthaux et al., 2007), which would make it at first sight poorly adapted to low H_4SiO_4 environment. Based on microcosm experiment, Brzezinski et al. (2011) showed that Fe and Si were associated with two different biogeochemical pathways with high dissolved Fe increasing growth rates and organic matter production, especially of large diatoms, while H_4SiO_4 availability would regulate diatom Si content. Our observations support the hypothesis that the strong decoupling between organic matter production and silicification in diatoms (Paasche, 1973; Brzezinski et al., 1990; McNair et al., 2018) may allow the development of large diatoms above the iron fertilized plateau, despite low H_4SiO_4 concentrations. By contrast, large and heavily silicified *Eucampia antarctica* cells were observed within the pycnocline gradient in addition to small *Chaetoceros* spp. *Hyalochaete* vegetative stages and CRS; with the former species overwhelming diatom C biomass and likely driving the formation of the DSM. During KEOPS, at the end of the chlorophyll seasonal peak, a diatom community shift was observed, from one dominated by *Chaetoceros* spp. *Hyalochaete* to a new one dominated by *E. antarctica* in the upper 100 m (Armand et al., 2008b). Hence, put together, these data suggest a late seasonal stage marked by the replacement of *E. antarctica* by *Corethron inerme* in the upper mixed layer, *E. antarctica* persisting below the MLD until late February before progressively disappearing. By early March, at the very end of the growing season, small *Chaetoceros* spp. *Hyalochaete* and their CRS became the main contributors to both abundances and carbon biomass in the deep layer. CRS were previously observed below the pycnocline in spring (Lasbleiz et al., 2016) and mid-summer (Armand et al., 2008b), which supports the hypothesis of their year-round presence, enabling the species to bloom first with the onset of favorable conditions in

spring (Lasbleiz et al., 2016). Resting spore formation is a strategy known to overcome unfavorable conditions such as low light levels (McQuoid and Hobson, 1996), macronutrients (Kuwata and Takahashi, 1990, 1999; Oku and Kamatani, 1995), or iron limitation (Sugie and Kuma, 2008). A recent study also showed that spores can be produced in nutrient-replete environments when a population reaches a threshold density and starts a process of self-removal from the water column (Pelusi et al., 2020). In our study, H_4SiO_4 depletion characterizing end-summer conditions is the most likely factor involved in triggering resting spore formation.

Outside the fertilized plateau, the remote diatom communities of the ML were very close with a dominance by *Fragilariopsis* species, *Cylindrotheca closterium*, and centric species belonging to the genera *Actinocyclus* and *Thalassiosira*. A common trait between off-plateau stations was the presence of *Fragilariopsis kerguelensis* below the ML, but its relative contribution was higher at M3 and M4, which supports that it is considered as an indicator of HNLC systems (Armand et al., 2008b; Lasbleiz et al., 2016). By contrast, within the pycnocline gradient, the two western diatom communities clustered separately from the eastern off-plateau community. The main differences were related to the dominance of *Chaetoceros atlanticus* on the western side, while it was virtually absent on the eastern side and replaced by CRS. The presence of the latter, known to characterize iron-fertilized systems (Abelmann et al., 2006; Armand et al., 2008b; Lasbleiz et al., 2016; Rembauville et al., 2016), tends to confirm that station M1 was at least partly influenced by the nearby plateau.

Three hypotheses can explain the presence of distinct diatom communities located either within the upper mixed layer or the pycnocline gradient: (1) the development of an active community supported by a deep nutricline, with diatoms adapted to low light levels (Crombet et al., 2011; Kemp and Villareal, 2013; Quéguiner, 2013), (2) the differential sinking and accumulation of diatoms from the overlying mixed layer (Quéguiner et al., 1997; Uitz et al., 2009), or (3) the selective grazing/parasitism. In a study similar to ours, investigating the link between microplankton community and particulate matter stoichiometry in the Kerguelen-Crozet region, Rembauville et al. (2016) suggested that high Si(OH)_4 diffusive fluxes were likely to sustain silicification in the transition layer (i.e. defined

as the interface between the stratified ocean interior and the highly turbulent surface mixed layer). Our incubation experiments with the fluorescent dye PDMPO showed on the contrary that silicification activity within the pycnocline gradient (≥ 100 m) was almost null, suggesting that deeper cells were not produced *in situ*, but rather originated from the overlying mixed layer. In particular, *Eucampia antarctica* cells and CRS observed above the plateau were not silicifying and likely corresponded to a remnant population that accumulated at the base of the mixed layer prior to the cruise. The relatively low percentage of crunched frustules (5 ± 3 %) suggests that selective grazing had little impact on shaping communities, while parasites could have controlled population dynamics prior to the cruise since elevated relative abundances of free Syndiniales spores was suggested by environmental sequencing (Sassenhagen et al., 2020). Hence, we argue that the density gradient acted as a strong physical barrier to sinking with variable impacts on species. Light species (e.g. *Cylindrotheca closterium*, *Corethron merriamii*, small *Fragilariopsis* spp.) were efficiently recycled in the ML and could not bypass the density gradient, whereas denser ones (e.g. *Fragilariopsis kerguelensis*, *Eucampia antarctica*, *Chaetoceros atlanticus*, CRS etc.) rapidly settled out of the mixed layer and accumulated in the pycnocline, leading to a vertical structure of diatom communities.

4.4 Differential impact of diatom species on Si/C export

Past studies in naturally and artificially Fe-fertilized systems have shown the central role played by phytoplankton community structure in carbon vs. silica export, advocating the need for a species-centred approach to understand the fine dynamics of biogeochemical fluxes (Smetacek et al., 2004; Salter et al., 2012; Assmy et al., 2013; Quéguiner, 2013; Rembauville et al., 2015b, 2016). While Assmy et al. (2013) coined the terms “Si sinkers” and “C sinkers” to characterize the roles of individual species in the coupling/uncoupling of Si and C biogeochemical cycles, Quéguiner (2013) distinguished two types of more or less silicified diatom communities on the basis of their different ecological niches marked by a different seasonality.

In the present study, heavily silicified *Fragilariopsis kerguelensis* were mostly observed as empty frustules below the mixed layer (D:I ratio $\gg 2$), which explains their low contribution to C biomass despite their high numerical abundances all over the study area. This species

was identified as a strong Si sinker during EIFEX artificial fertilization experiment by Assmy et al. (2013) who reported a steady and downward flux of empty *F. kerguelensis* frustules, inside and outside the Fe-fertilized patch, associated with low-level, quasi-constant mortality. Indeed, *F. kerguelensis* frustules are thick and heavily silicified (Si:N ratios > 4:1) (Hamm et al., 2003; Hoffmann et al., 2007; Wilken et al., 2011), which has led to the hypothesis of a coevolution with copepods to withstand grazing pressure (the “arms race” – Smetacek et al., 2004). Unexpectedly and contrary to the conceptual approaches of Assmy et al. (2013) and Quéguiner (2013), we observed many crunched *Fragilariopsis kerguelensis* frustules (average per station: 9-20 %) as well as copepod faecal pellets containing fragmented frustules (see supplementary Figure S9) which indicates that *Fragilariopsis* cells had been processed by copepod mandibles. In addition, we also frequently observed whole *F. kerguelensis* cells inside phaeodarians belonging to the genus *Protocystis* spp. (e.g. *P. swirei*, *P. harstoni*, *P. tridens*; see supplementary Figure S9), which is consistent with the results of González (1992) who found *Fragilariopsis* as the most frequent diatom genus present in phaeodarian minipellets in spring in the Weddell–Scotia confluence. Selective grazing on *F. kerguelensis* likely increased the number of detrital cells, enhancing the sinking of Si relative to C. The preferential exportation of Si over other nutrients by thick-shelled empty frustules then strongly fuels the Si pump (Dugdale et al., 1995), explaining the extremely high Si:C and Si:N ratios we report below the MLD. Our hypothesis is supported by a significant correlation between BSi:POC and D:I ratios (Spearman rank correlation: $n = 64$, $\rho = 0.67$, $p < 0.05$), and the much higher residual NO_3^- (> 21 $\mu\text{mol L}^{-1}$) relative to H_4SiO_4 (range: 1.7-6.9 $\mu\text{mol L}^{-1}$) concentrations in the surface layer. Outside the plateau, the Si pump was obviously more efficient due to (1) the higher proportion of *F. kerguelensis* below the ML, and (2) the physiological response to iron stress further increasing their silicification degree. Our results are similar to those from Rembauville et al. (2016) who showed that Southern Ocean transition layers (i.e. the pycnocline gradient) are key areas of C and Si decoupling where empty diatom frustules mainly from *F. kerguelensis* and *Pseudo-nitzschia* accumulate. During austral summer, at the peak of the plateau bloom development, Mosseri et al. (2008) also demonstrated that both the Fe-fertilized plateau and surrounding Fe-depleted waters behaved as Si pumps but based upon different mechanisms with contrasted intensities. In the HNLC area, the Si pump was mainly driven by the development of more heavily silicified diatoms, whereas above the Kerguelen Plateau, the Si pump was mainly

driven by the preferential degradation of soft organic matter over BSi dissolution. Apart from *F. kerguelensis*, several taxa such as *Actinocyclus/Thalassiosira* spp., *Pseudo-nitzschia* spp., and *Chaetoceros atlanticus* displayed D:I ratios > 2 , although their influence on the Si pump was probably weaker. By contrast, *Chaetoceros* spp. vegetative stages and CRS displayed D:I ratios < 0.5 , indicating that many cells were still intact below the mixed layer. Heavily silicified CRS can contain up to 10 times more carbon than the vegetative forms (Kuwata et al., 1993), have no vacuole and are rich in lipids and carbohydrates (Doucette and Fryxell, 1983; Kuwata et al., 1993), which make them efficient vectors for C and Si export. Above the plateau, CRS were abundant below the ML (Figure 8) and were associated with a quasi constant C biomass between 100 and 200 m (Figure 6), suggesting they efficiently bypassed the pycnocline discontinuity and carried C to deeper layers. These results are in line with sediment trap and surface-sediment core studies, which have reported CRS as one of the main vector of carbon export in naturally iron fertilized systems, in particular over the Kerguelen Plateau and downstream of South Georgia where they can contribute to 42-52 % of the annual POC fluxes (Armand et al., 2018a, Rembauville et al., 2015b, 2016, 2018). In our study, *Eucampia antarctica* D:I ratio fell between the thresholds >0.5 and <2 at M2-1, meaning the species was almost equally represented by intact and detrital cells below the ML. Nevertheless, it was likely an important vector of carbon export, since most of the diatoms sampled by the Bottle-Net device belonged to this species (47 % within the 100-450 m layer; Leblanc et al., in prep). During the naturally iron-fertilized Crozet bloom (CROZEX project), a significant positive relationship was reported between POC fluxes and *E. antarctica* by sediment traps deployed at 2000 m, highlighting the importance of this species for carbon export (Salter et al., 2012). Hence, our data show that some species were able to efficiently bypass the pycnocline and to carry C/Si to the ocean twilight zone. Through their physiological state, life stages, and selective grazing by micro/mesozooplankton, they can influence the efficiency of the export, as well as the properties of the sinking particles.

Conclusion

Our ability to predict the future role of the ocean in modulating the global C cycle and ultimately controlling the evolution of global climate depends on our understanding of the functioning of the biological carbon pump. The latter still presents major gaps, especially in the knowledge of the relationships that exist between the oceanic biodiversity and the

efficiency of carbon transfer to deep layers, which is partly reflected by the relative utilization of associated elements, in particular N and Si in the Southern Ocean. During the MOBYDICK expedition, south of the Kerguelen Islands, we studied the processes linking diatom diversity with biogeochemistry, at several contrasted sites differently impacted by iron availability. Outside the iron-fertilized plateau, iron stress led to the selection of more heavily silicified taxa while a direct response to iron stress further increased the silicification degree of these selected diatoms. This affected the properties of the bulk particulate matter, which was characterized by higher elemental Si:C and Si:N ratios when compared to the plateau. Upper mixed layer diatom communities were clearly different between on- and off-plateau stations. Above the plateau, large and weakly silicified *Corethron inerme* were able to grow despite low silicic acid concentrations ($< 2.7 \mu\text{mol L}^{-1}$) characteristic of the end stage of phytoplankton development, accompanied with *Actinocyclus/Thalassiosira* spp. and the pennate species *Thalassionema nitzschioides* and *Cylindrotheca closterium*. In HNLC waters, the diatom community was different and mainly composed of *Fragilariopsis* species, *Cylindrotheca closterium*, and the centric genera *Actinocyclus/Thalassiosira* spp. Beside horizontal spatial heterogeneity, depth turned out as an important parameter shaping diatom communities, since a deep and inactive community associated with the pycnocline gradient was systematically observed carrying organic matter (C, N) and biogenic minerals (Si) below the mixed layer. In particular, outside the plateau, the heavily silicified species *Fragilariopsis kerguelensis* carried mostly Si since it was largely found as detrital frustules, this being partly caused by a strong grazing pressure by micro- and mesozooplankton. Conversely, above the plateau, many *Eucampia antarctica* and *Chaetoceros* spp. cells (resting spores and vegetative stages) were still intact below the mixed layer, hence carrying both Si and C to the deeper layers.

Our study highlights the importance of species-specific properties (e.g. morphology, silicification degree, carbon content, etc.), along with their physiological state (here related to iron availability), their life stages, and entire ecosystem trophodynamics including selective grazing in determining the efficiency of the export and the biogeochemical properties of exported particles, as emphasized by Tréguer et al. (2018). In the context of a changing Southern Ocean (e.g. greening, acidification, etc.), we advocate for the need to develop more studies following a species centered approach, as well as assessing trophic

interactions through trophodynamics (e.g. predation, parasitism, saprophytism, etc.) in order to finely resolved biogeochemical fluxes and their control mechanisms. This should help to extract synthetic descriptors to better constrain more complex biogeochemical models aimed at simulating more closely the biological pump of carbon under the perspective of global climate change.

Acknowledgements

We thank B. Quéguiner, the PI of the MOBYDICK project, for providing us the opportunity to participate to this cruise, the chief scientist I. Obernosterer and the captain and crew of the R/V Marion Dufresne for their enthusiasm and support aboard during the MOBYDICK–THEMISTO cruise (<https://doi.org/10.17600/18000403>). This work was supported by the French oceanographic fleet (“Flotte océanographique française”), the French ANR (“Agence Nationale de la Recherche”, AAPG 2017 program, MOBYDICK Project number : ANR-17-CE01-0013), and the French Research program of INSU-CNRS LEFE/CYBER (“Les enveloppes fluides et l’environnement” – “Cycles biogéochimiques, environnement et ressources”).

Conflict of interest

We declare that all authors of this manuscript do not have any conflict of interest.

Figures

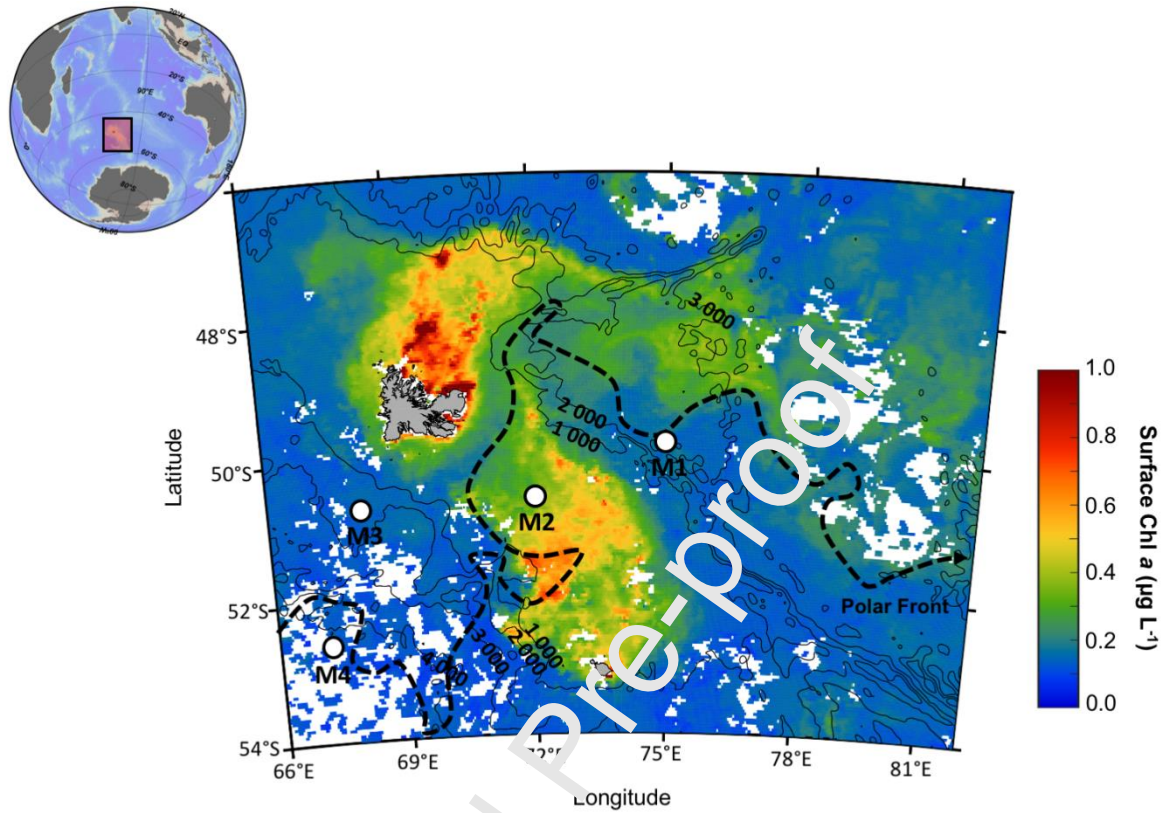


Figure 1. Location of the Kerguelen Plateau in the Indian sector of the Southern Ocean and detailed map of the satellite-derived surface chlorophyll *a* concentration (MODIS level 3 product) averaged over March 2018. The four stations sampled during MOBYDICK are indicated. Contour lines represent the bathymetry (m). The dotted line represents the position of the Polar Front (P.F.) according to Pauthenet et al. (2018).

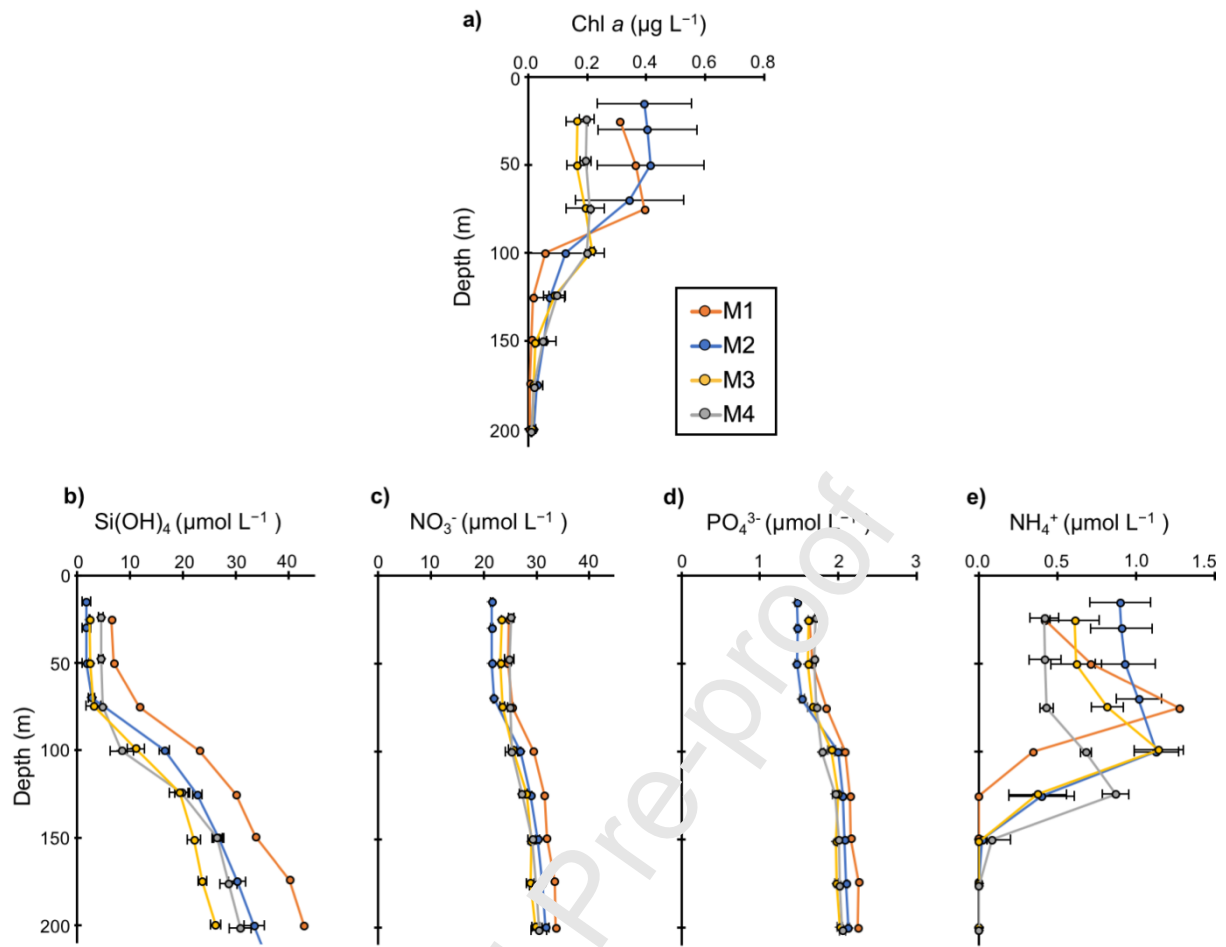


Figure 2. Average profiles of Chl *a* (a) and nutrients (b-e) from several visits at the four stations.

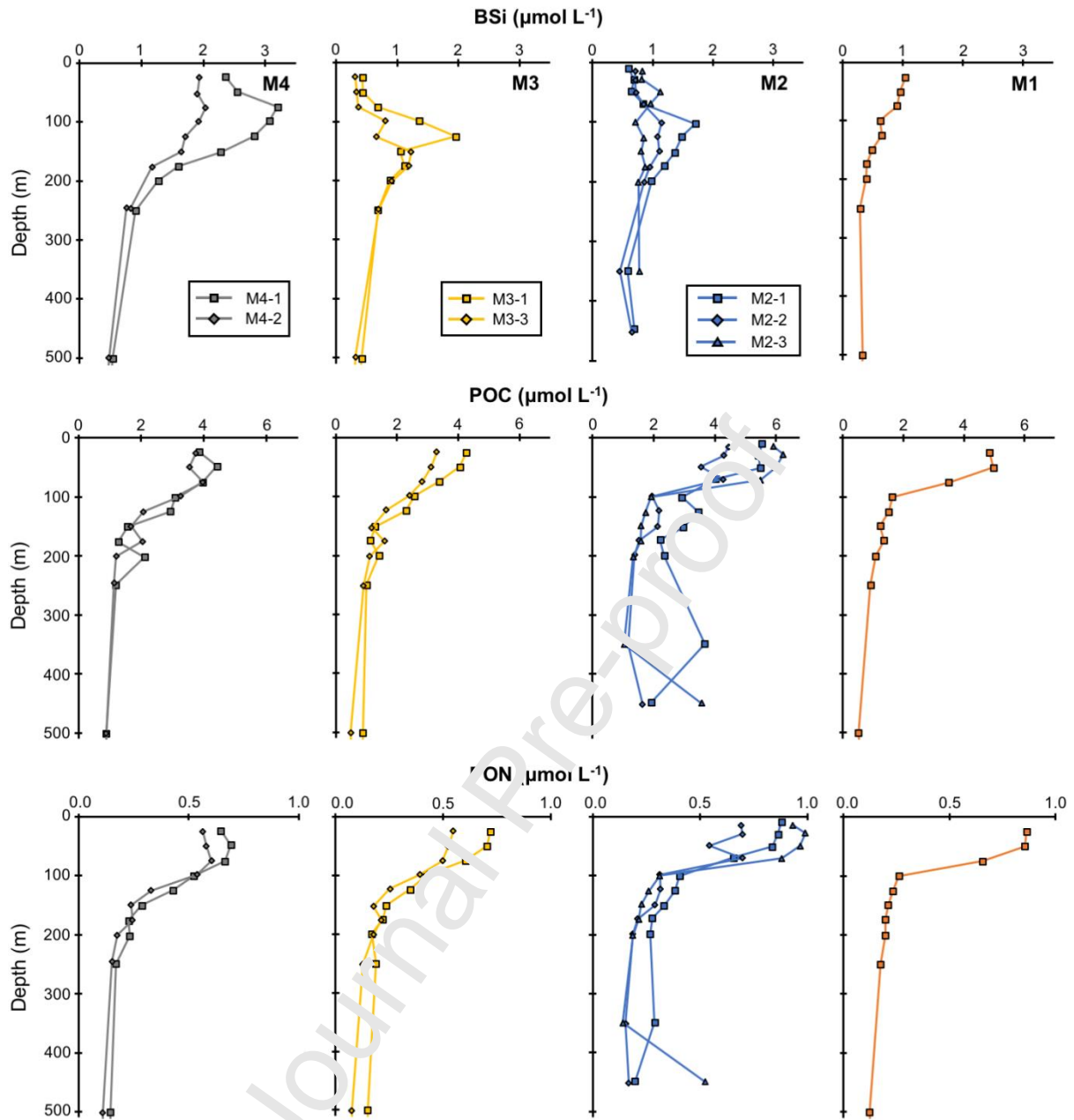


Figure 3. Vertical distribution of biogenic silica (BSi), particulate organic carbon (POC), and particulate organic nitrogen (PON) at the four stations. Data are expressed in $\mu\text{mol L}^{-1}$. Symbols correspond to repeated visits to a same station.

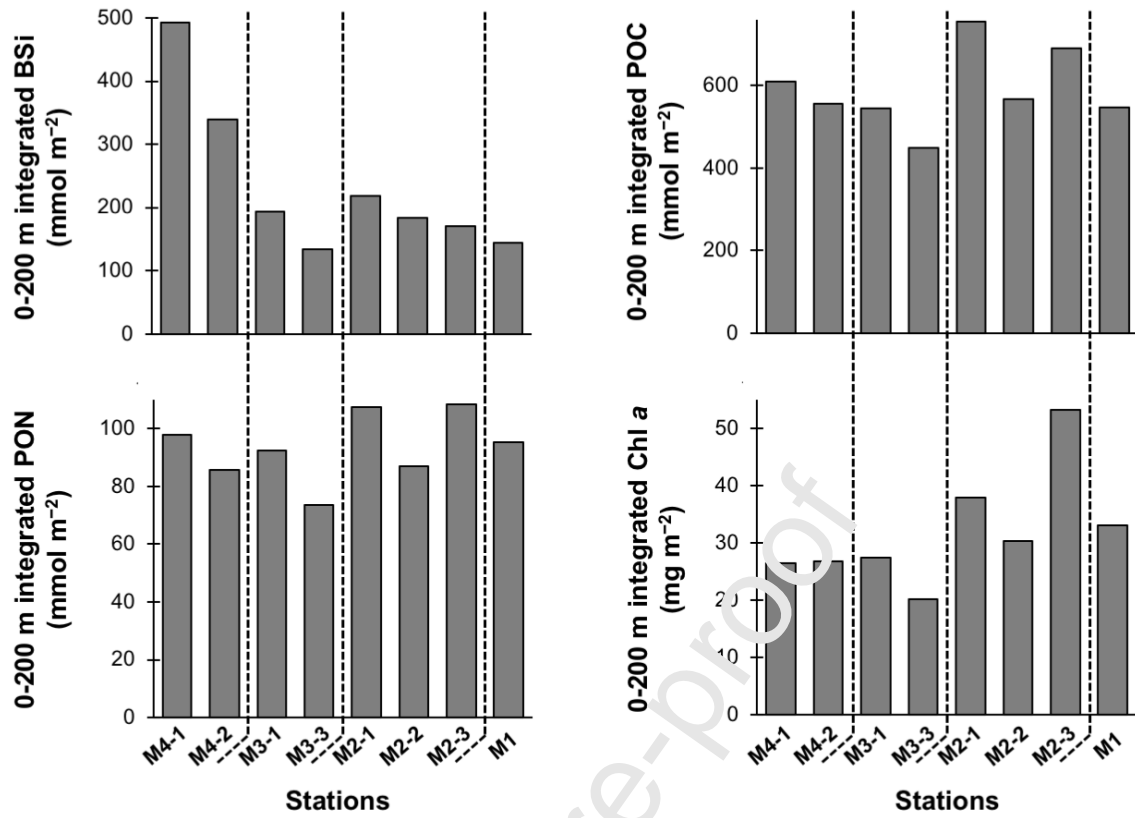


Figure 4. Integrated BSi, POC, PON, and Chl *a* concentrations between 0 and 200 m at the four stations.

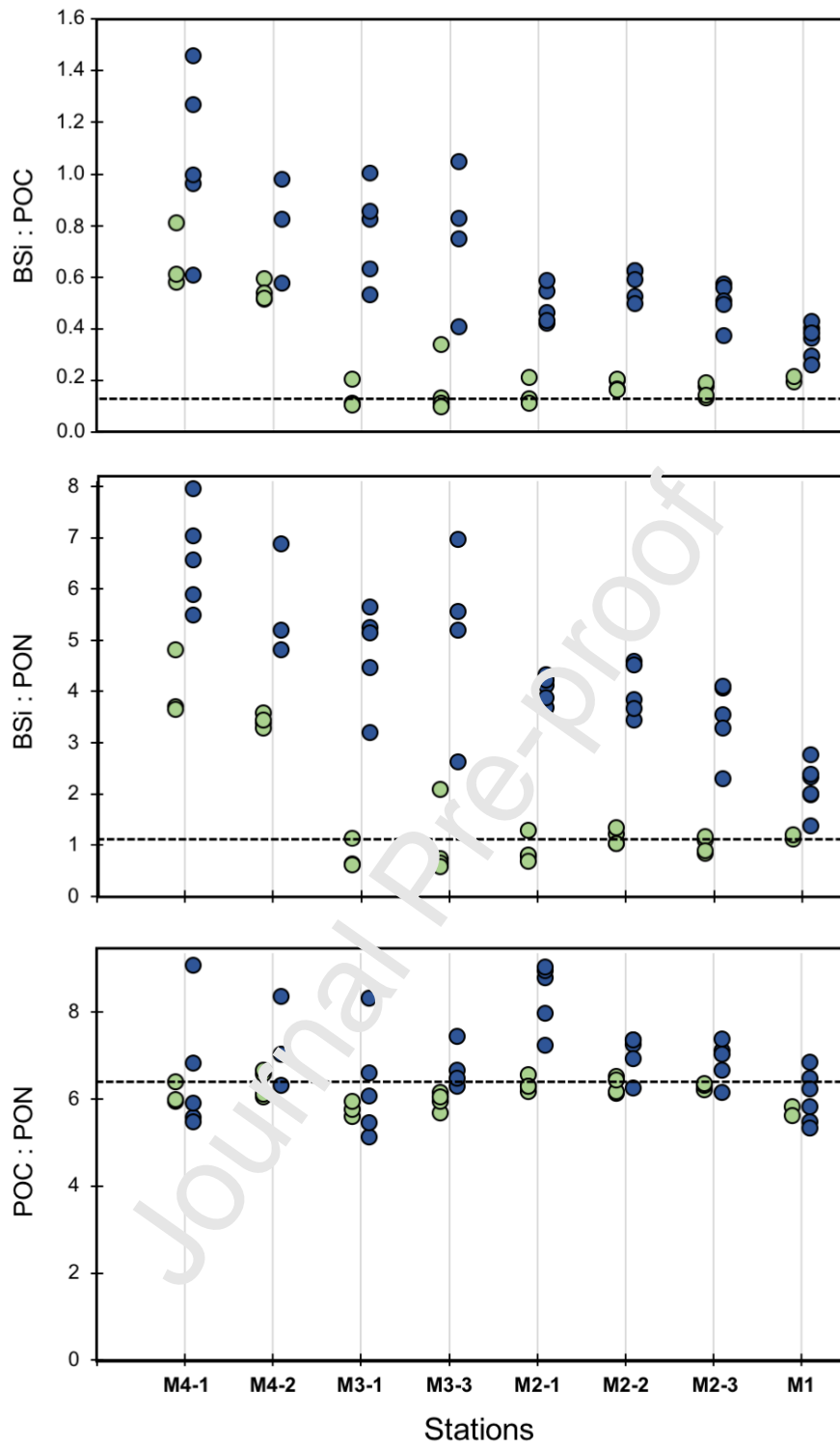


Figure 5. BSi:POC, BSi:PON, and POC:PON molar ratios based on the bulk of particulate matter between 0-MLD (green dots) and MLD-200 m (blue dots) at the four stations.

The black dashed lines represent the empirical values of Si:C (0.13), and Si:N (1.12) for nutrient-replete diatoms reported by Brzezinski (1985), as well as the typical value of C:N (6.6) reported by Redfield et al. (1963).

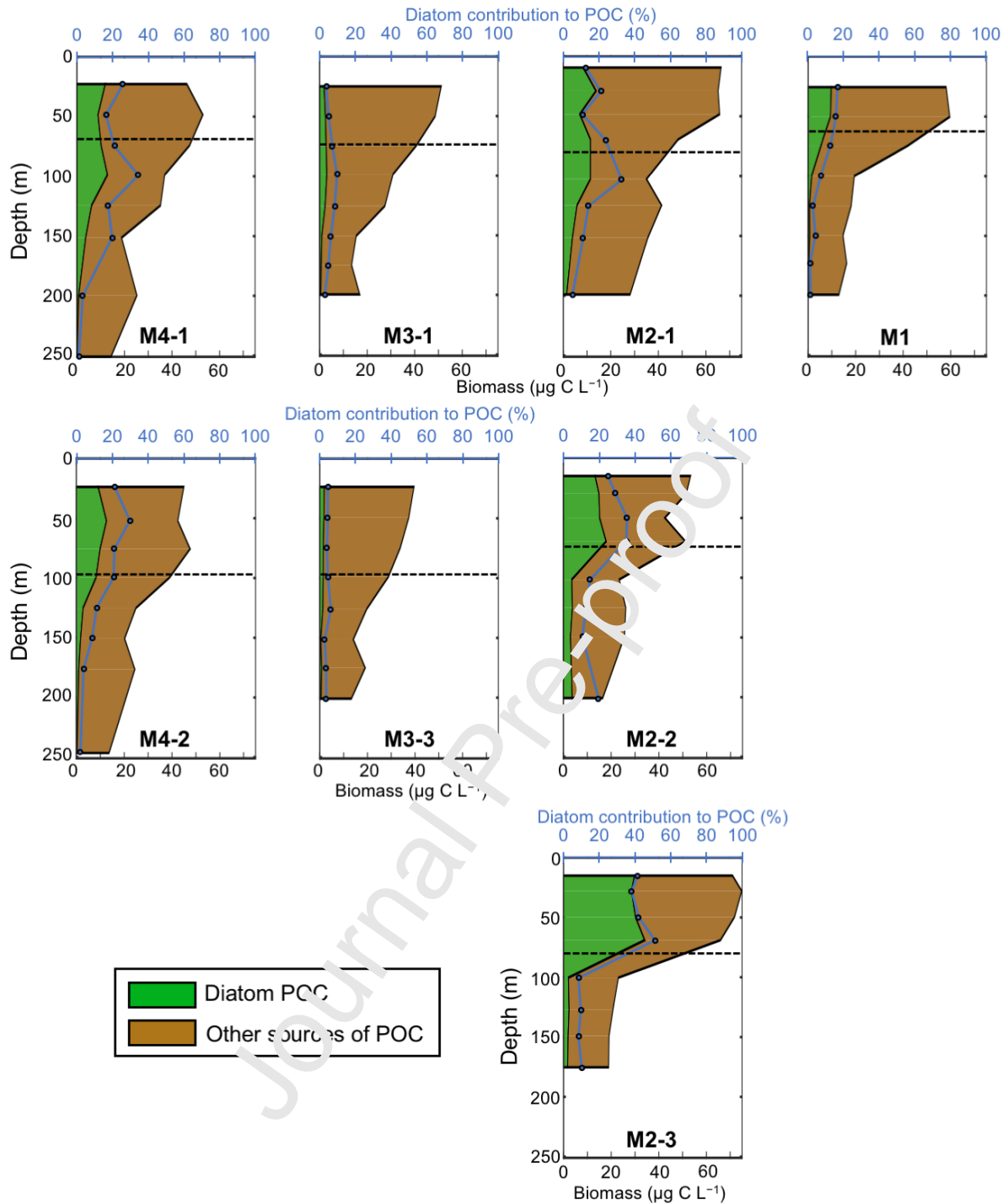


Figure 6. Absolute diatom C biomass and its contribution to POC.

Absolute diatom carbon biomass (green area) and other sources of POC (brown area). The sum of the green and brown areas gives the total POC. Data are expressed in $\mu\text{g C L}^{-1}$. Blue dots indicate the diatom contribution to total POC (in percent). The dashed line indicates the location of the mixed layer depth (MLD).

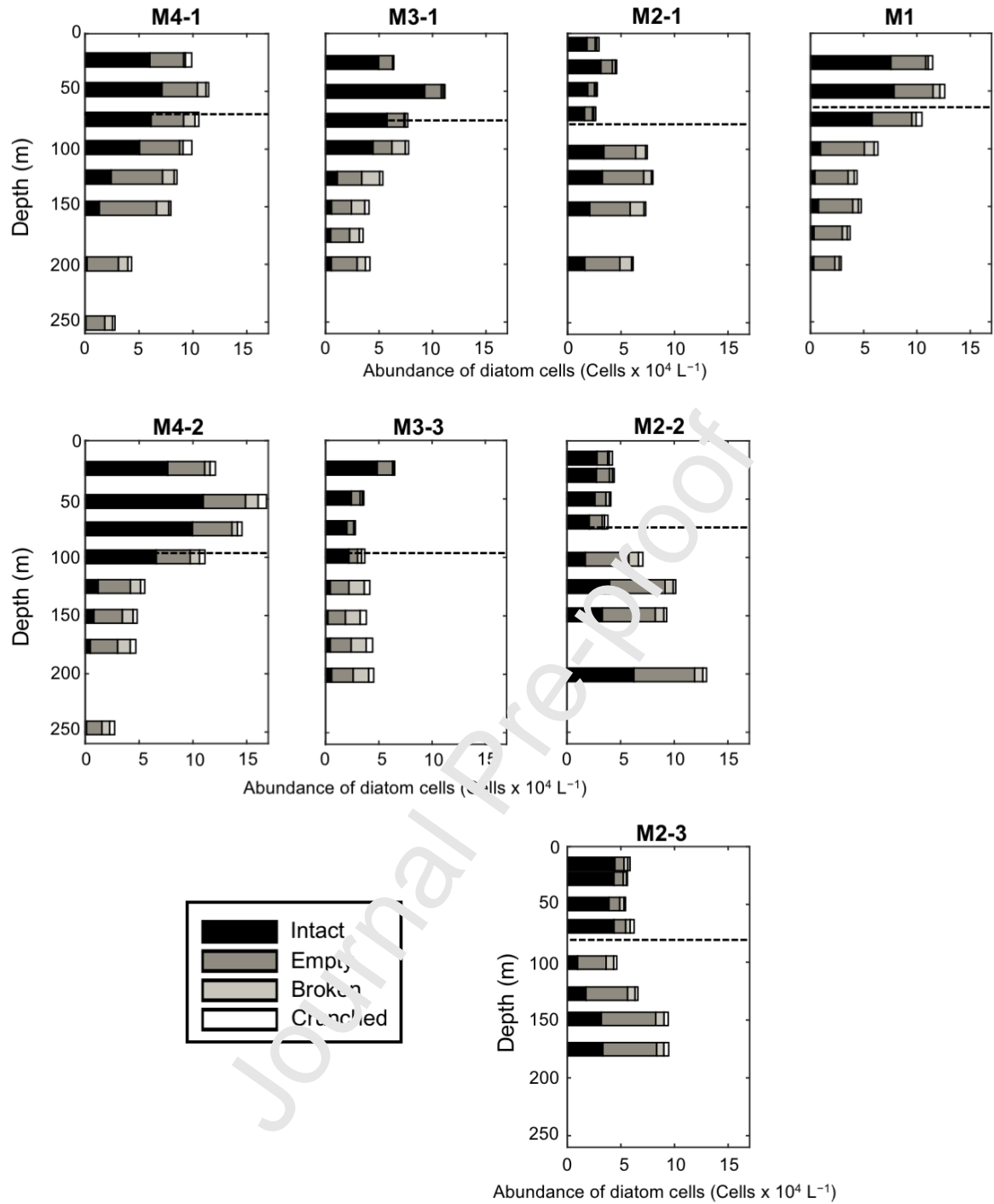


Figure 7. Vertical distribution of intact and detrital (i.e. empty, broken, and crunched) frustule abundances.

The dashed line indicates the location of the MLD.

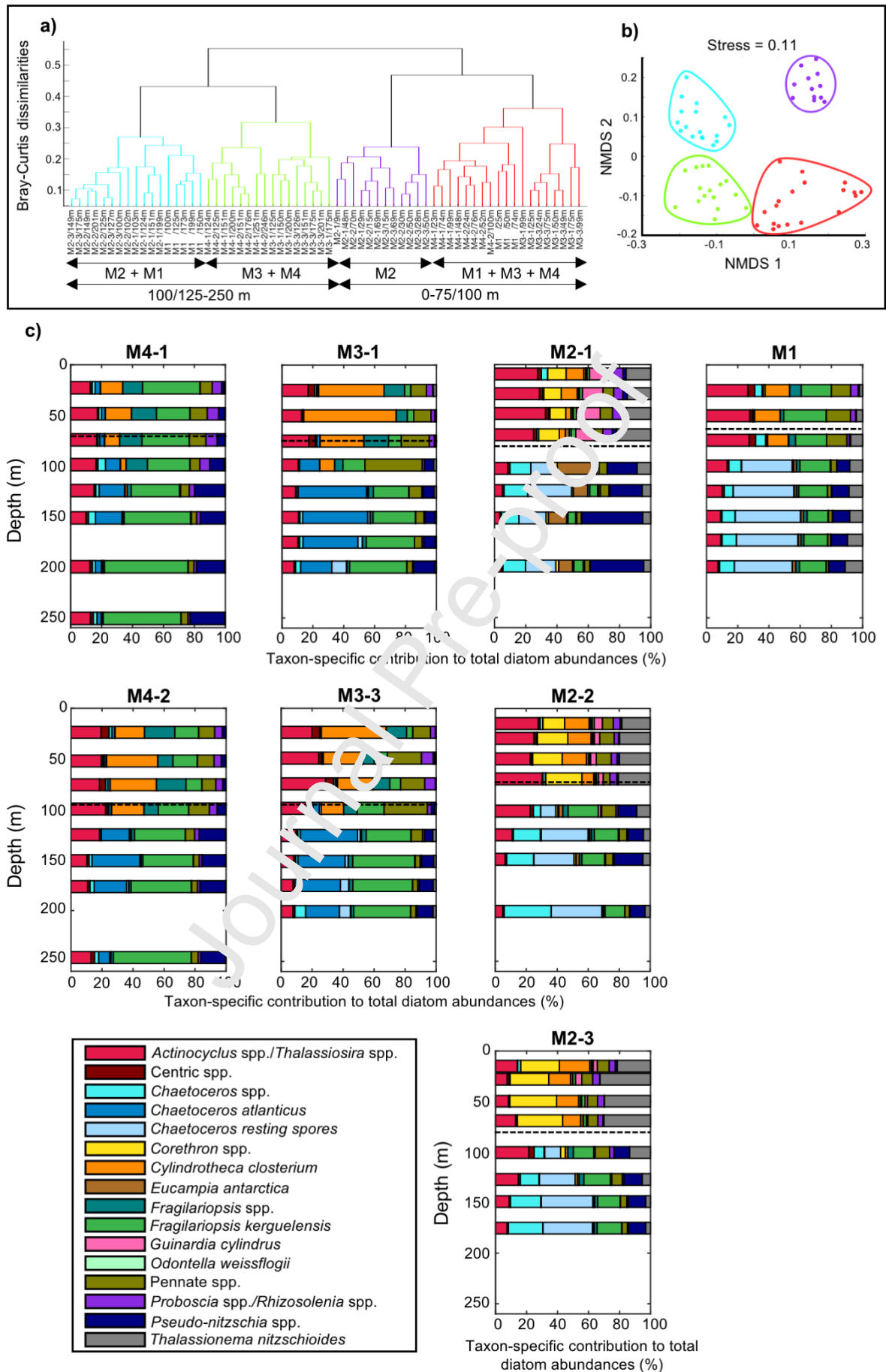


Figure 8. Community structure and taxon-specific contribution to total diatom abundances.

(a) Cluster analysis performed on $\log(x+1)$ abundances. The dendrogram displays the similarity relationship among samples in terms of their taxonomic composition. (b) Non-metric multidimensional scaling (NMDS) ordination plot. Stations are coloured according to the cluster they belong to. (c) Taxon-specific contribution to total diatom abundances. Total abundances include both intact and detrital cells. Taxa are mutually exclusive, e.g. *Chaetoceros* spp. include all *Chaetoceros* species, excluding *C. atlanticus* and CRS. The dashed line indicates the location of the MLD.

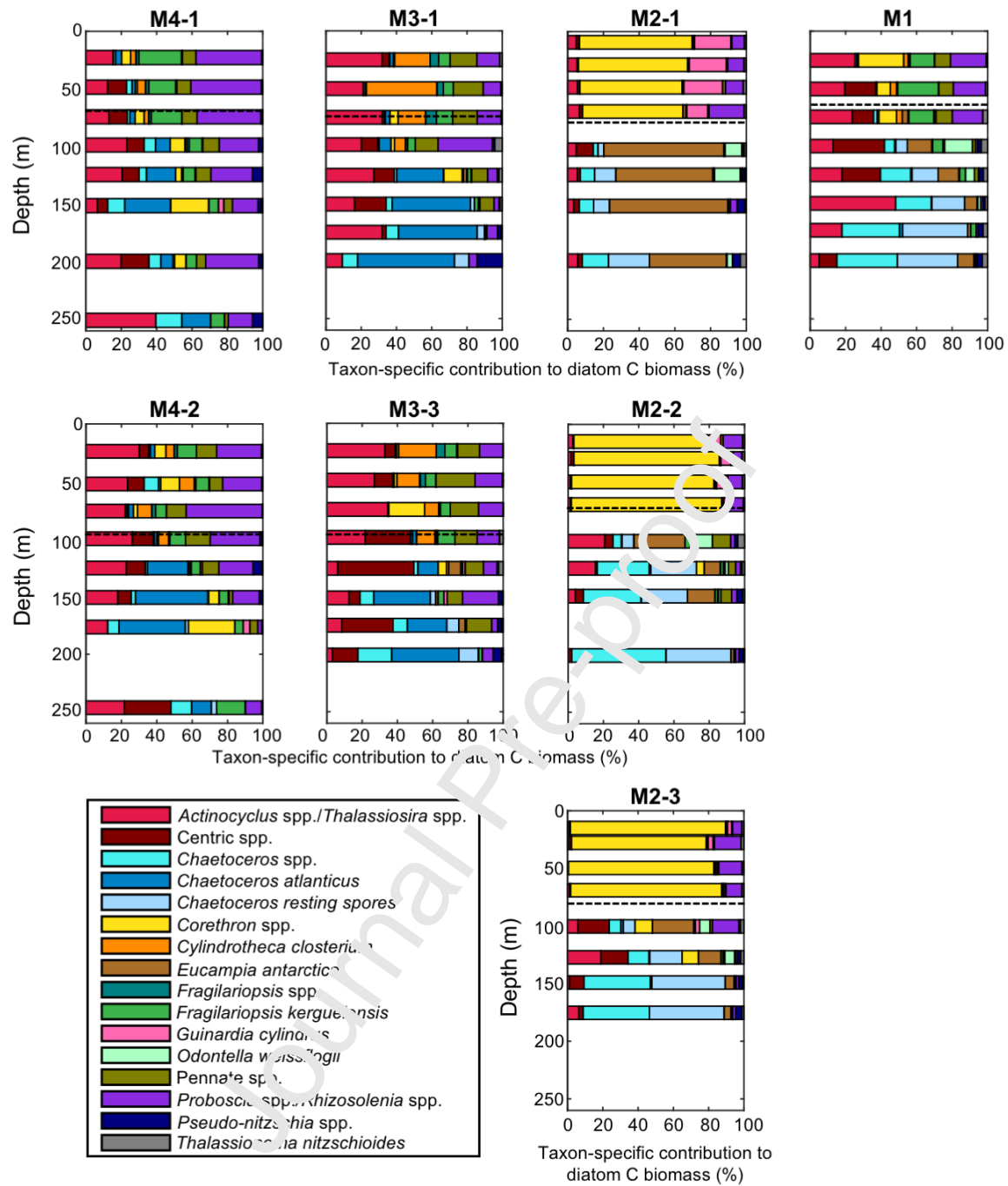


Figure 9. Taxon-specific contribution to diatom carbon biomass.

The dashed line indicates the location of the MLD.

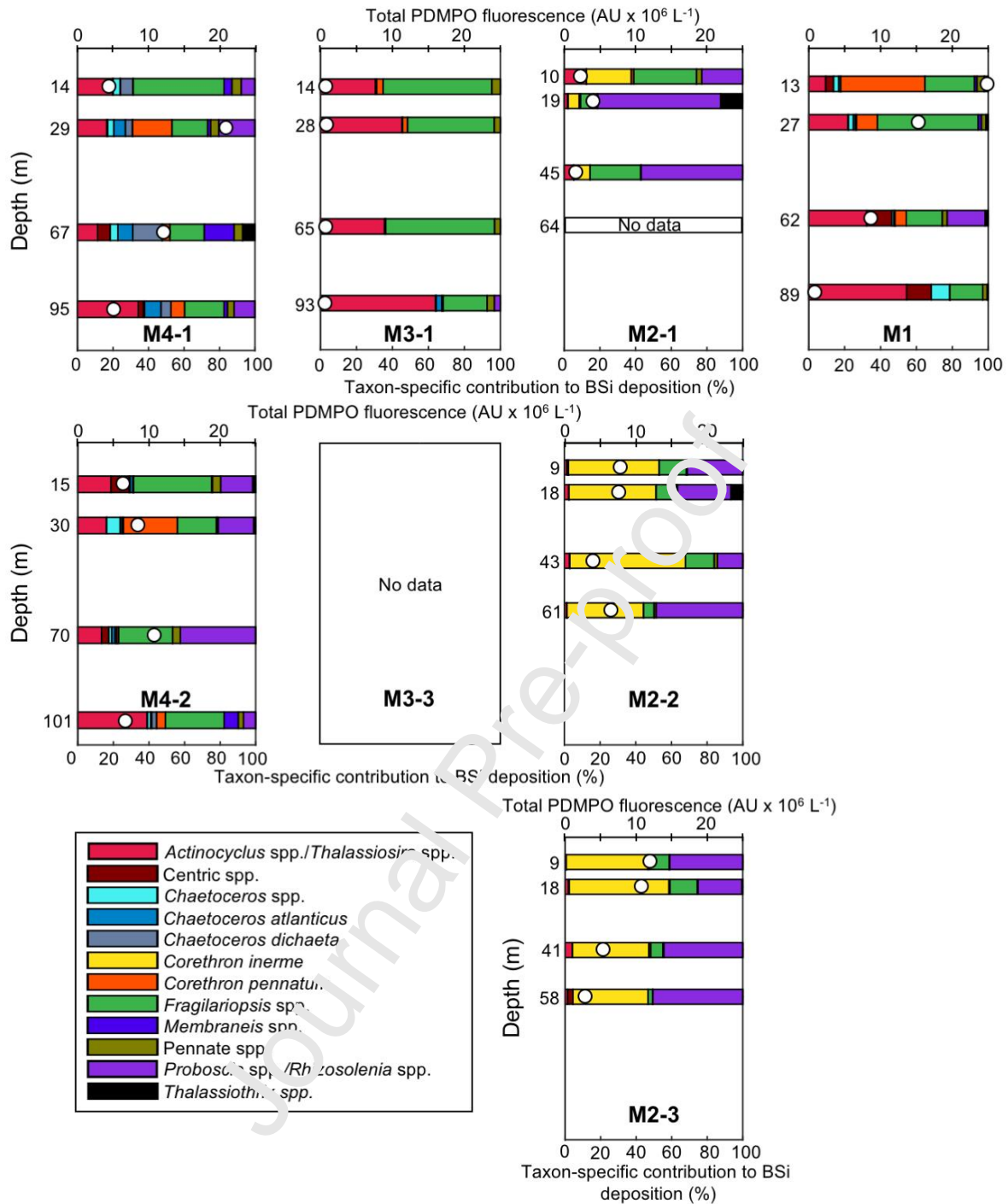


Figure 10. Community silicification activity and taxon-specific contribution to biogenic silica deposition, based on PDMPO staining.

White dots correspond to the total PDMPO fluorescence (AU x 10⁶ L⁻¹), i.e. the sum of each taxa absolute fluorescence. Collection depths were adjusted to correspond to simulated irradiance depths, which were equal to 50 %, 25 %, 4 %, and 1 % of the surface PAR. Samples collected deeper and incubated in the dark did not fluoresce and therefore are not presented. Colour code and taxa presented are intentionally different from Figure 8 and 9 to

show taxa that were important contributor to BSi deposition, while they were not dominant to abundances and/or C biomass. No data are reported for station M3-3 due to technical problems during incubations.

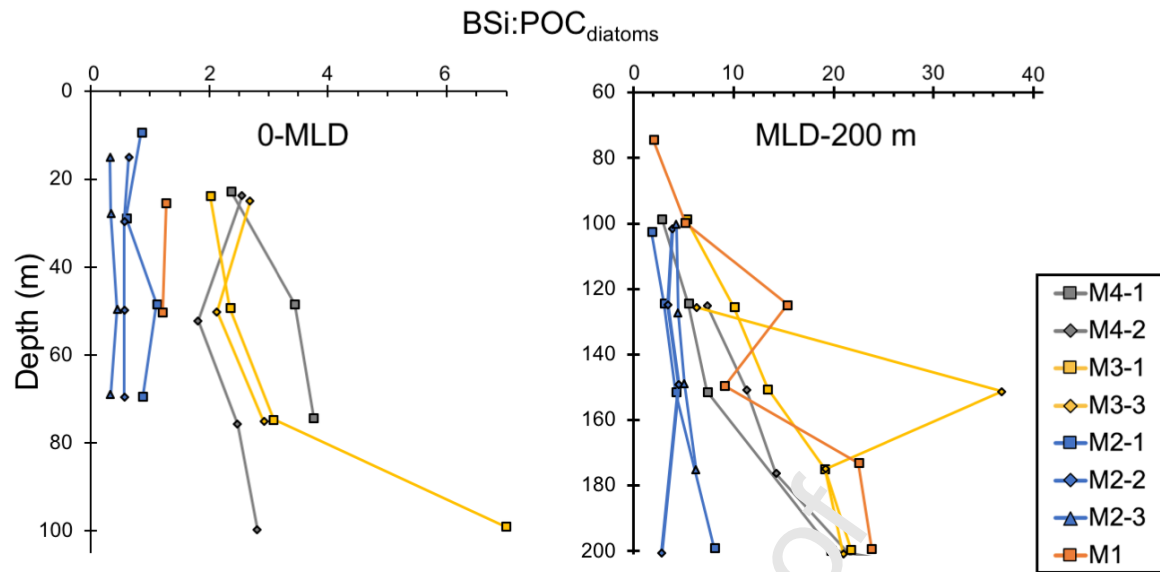


Figure 11. Vertical profiles of $\text{Si:C}_{\text{diatom}}$ ratios between 0-MLD (left panel) and MLD-200 m (right panel). This ratio is based on calculated diatom carbon biomass rather than the bulk POC measurements.

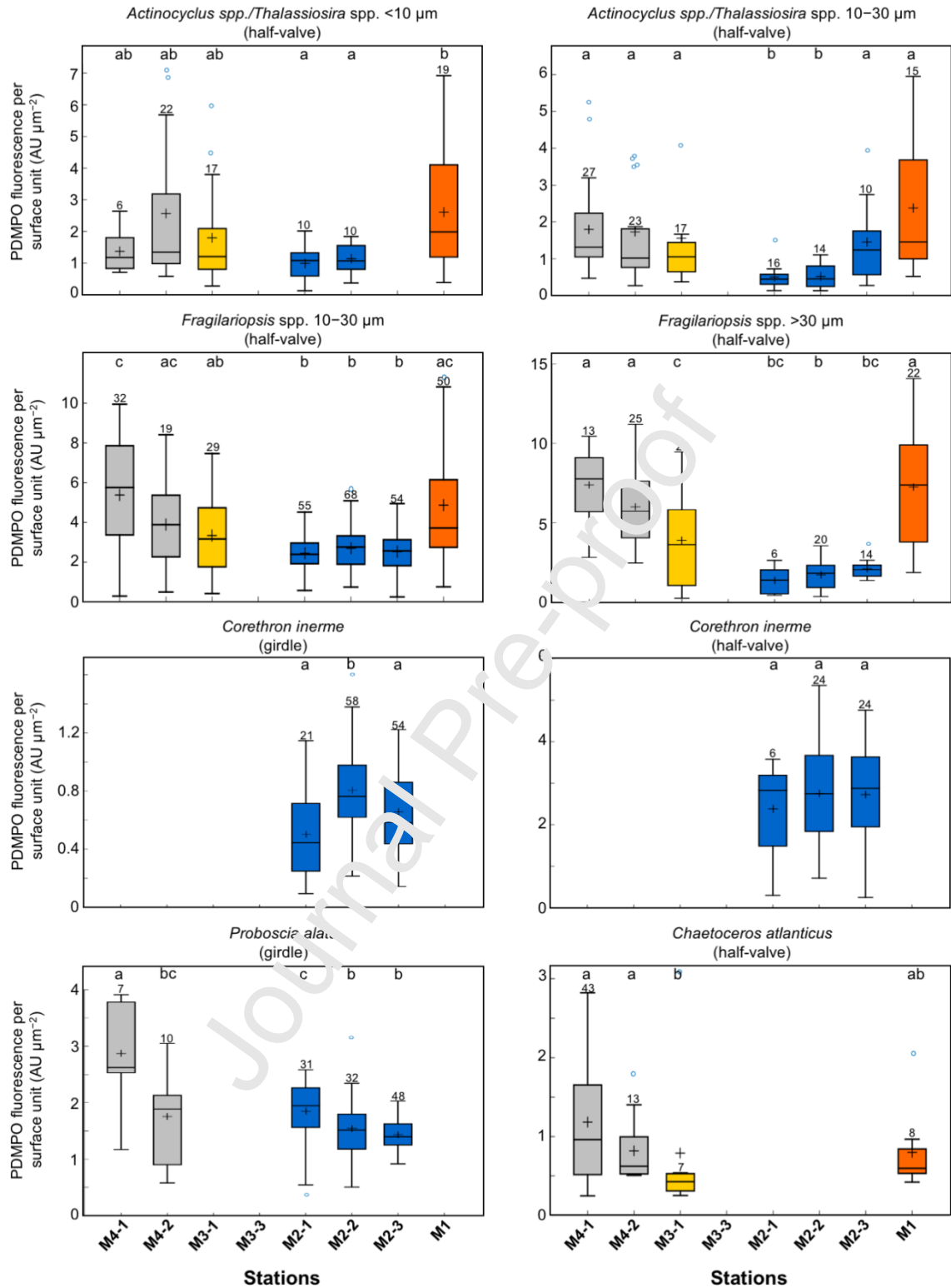


Figure 12. Silicification degree estimated through PDMPO staining.

Taxa presented are the most actively silicifying ones. The bottom and top edges of the box indicate the 25th and 75th percentiles, respectively. The line inside the box and the asterisk represent the median and the mean, respectively, and were calculated based on the data

from all incubation depths. The vertical lines extend to the minimum and maximum values, while blue dots correspond to outliers. The number of observations for each box is indicated above the vertical line. Boxplot of which medians are not statistically different are indicated by the same letter (Mann-Whitney u test, $p > 0.05$).

Tables

Table 1. Metadata and hydrographical conditions at stations sampled during the MOBYDICK expedition.

Station	Latitude/Longitude	Date	Bottom depth (m)	MLD (m)	Ze 1% (m)
M4-1	52.60°S, 67.20°E	01/03/2018	4 731	69	95
M4-2		12/03/2018		96	101
M3-1	50.68°S, 68.06°E	04/03/2018	1730	74	93
M3-3		19/03/2018		96	105
M2-1	50.62°S, 72.00°E	26/02/2018	520	79	64
M2-2		05/03/2018		73	61
M2-3		16/03/2018		80	58
M1	49.85°S, 74.90°E	09/03/2018	2 723	63	89

Table 2. Average detrital:intact frustules ratios (D:I) below the MLD. Number in brackets correspond to the standard deviations. "Ab" corresponds to the relative abundance averaged below the MLD. Bold numbers represent numerically dominant taxa below the mixed layer depth, i.e. with a relative contribution to total diatom abundances higher than 10 %.

Species and genera grouping	M4-1		M4-2		M3-1		M3-3		M2-1		M2-2		M2-3		M1	
	D:I	Ab	D:I	Ab	D:I	Ab	D:I	Ab	D:I	Ab	D:I	Ab	D:I	Ab	D:I	Ab
<i>Fragilariopsis kerguelensis</i>	58.6 (71.3)	41	51.1 (35.3)	39	64.5 (55.7)	27	221.8 (57.5)	36	63.6 (79.5)	4	89.5 (84.7)	16	113.4 (81.7)	15	134.2 (126.8)	17
<i>Chaetoceros</i> resting spore	0.3 (0.3)	0	0.3 (0.3)	1	1.1 (1.5)	3	1.4 (0.3)	4	0.5 (0.1)	20	0.4 (0)	25	0.7 (0.1)	25	7.5 (1.4)	32
<i>Pseudo-nitzschia</i> spp.	34.2 (44.2)	17	74.6 (97.8)	16	6.2 (4.5)	8	9.4 (3.2)	8	13.3 (3.9)	28	1.1 (3.7)	13	12.7 (2.7)	11	20.4 (13.3)	9
<i>Actinocyclus/Thalassiosira</i> spp.	24.4 (28.3)	13	26.8 (18.2)	13	20.4 (14.6)	10	28 (8.5)	8	10.2 (8.1)	5	50.1 (72.4)	11	29.4 (19.9)	13	24.2 (17.7)	13
<i>Chaetoceros atlanticus</i>	2.2 (2.6)	10	3.4 (3.6)	19	3.3 (0.3)	31	8.7 (2.7)	29	- (-)	0	1.2 (0.7)	0	2 (1.7)	0	1 (0.5)	0
<i>Chaetoceros</i> spp.	1.9 (2.2)	3	0.5 (0.3)	2	0.8 (0.6)	2	0.7 (0.2)	3	0.6 (0.1)	14	0.4 (0.1)	17	0.5 (0.1)	15	1.1 (0.7)	8
<i>Pennate</i> spp.	18.7 (25)	5	67 (97.3)	4	23.9 (30.6)	12	17.3 (16.5)	4	24.9 (24.4)	4	30.8 (23)	5	31 (28.3)	6	5.7 (5.3)	4
<i>Thalassionema nitzschioides</i>	1.2 (0.7)	0	2.3 (1.5)	0	2.6 (1.8)	1	6.4 (3.5)	2	2 (0.9)	6	4.2 (1.2)	5	6.6 (1.2)	6	11 (8.2)	9
<i>Eucampia antarctica</i>	- (-)	0	- (-)	0	0.1 (0.1)	0	0.4 (0.2)	0	1.5 (1.6)	13	2.2 (2.3)	2	1.2 (0.9)	1	17.1 (24.1)	2
<i>Fragilariopsis</i> spp.	12.9 (20)	4	18.4 (8)	1	11 (13.4)	3	62 (-)	2	28.1 (24.4)	1	51.6 (25.9)	2	59.8 (56.9)	3	8.7 (6.8)	2
<i>Corethron inerme</i>	2.6 (3.7)	0	1.3 (0.3)	0	1.3 (1.1)	0	- (-)	0	- (-)	2	16.8 (-)	1	28.2 (22.3)	1	3.7 (-)	0
<i>Cylindrotheca closterium</i>	0.9 (1.4)	1	1 (1.4)	0	0.4 (0.5)	2	0.1 (0.1)	0	- (-)	0	0.1 (0.2)	0	0 (0)	0	0 (0)	2
<i>Proboscia/Rhizosolenia</i> spp.	2.6 (2.4)	3	4.1 (2.1)	2	2.8 (2.3)	1	3.9 (0.9)	1	5.4 (2.7)	0	5.6 (0.9)	1	5.4 (2.8)	1	9.6 (7.2)	0
Centric spp.	11.8 (14.5)	1	12.3 (14.5)	1	11.6 (17.1)	1	12 (10.9)	1	15.8 (2.1)	1	19.7 (9.5)	1	13.6 (16.4)	2	13.6 (10.5)	1
<i>Guinardia cylindrus</i>	6 (7.8)	0	1.7 (1.2)	0	3 (2.8)	0	3 (2.8)	0	8.3 (7.4)	1	6.9 (4.7)	1	6.6 (5.1)	0	1 (1.4)	0
<i>Odontella weissflogii</i>	- (-)	0	- (-)	0	- (-)	0	- (-)	0	3.2 (3.7)	1	1.6 (1.3)	0	0.7 (0.2)	0	0.8 (0.9)	0

References

- Abelmann A, Gersonde R, Cortese G, Kuhn G, Smetacek V. 2006. Extensive phytoplankton blooms in the Atlantic sector of the glacial Southern Ocean. *Paleoceanography* **21**(1): PA1013. doi: 10.1029/2005PA001199
- Afnor, 2015. EN 16695. Water Quality - Guidance on the estimation of phytoplankton biovolume. *Afnor*, 1-109
- Allredge AL, Gotschalk CC. 1989. Direct observations of the mass flocculation of diatom blooms: characteristics, settling velocities and formation of diatom aggregates. *Deep Sea Res Part Oceanogr Res Pap* **36**(2): 159–171. doi: 10.1016/0198-0149(89)90131-3
- Allredge AL, Jackson GA. 1995. Preface: Aggregation in marine system. *Deep Sea Res Part II Top Stud Oceanogr* **42**(1): 1–7. doi: 10.1016/0967-0645(95)90003-9
- Aminot A, K  rouel R. 2007. Dosage automatique des nutriments dans les eaux marines : m  thodes en flux continu. Editions Quae, Ifremer, Brest - France, 189 pp.
- Armand L, Crosta X, Qu  guiner B, Mosseri J, Garcia N. 2008a. Diatoms preserved in surface sediments of the northeastern Kerguelen Plateau. *Deep Sea Res Part II Top Stud Ocean* **55**(5–7): 677–692. doi: 10.1016/j.dsr2.2007.12.032
- Armand L, Veronique C-F, Mosseri J, Qu  guiner B. 2008b. Late summer diatom biomass and community structure on and around the naturally iron-fertilised Kerguelen Plateau in the Southern Ocean. *Deep Sea Res Part II* **55**(5–7): 653–676. doi: 10.1016/j.dsr2.2007.12.031
- Armstrong RA, Lee C, Hedges JL, Honjo S, Wakeham SG. 2002. A new, mechanistic model for organic carbon fluxes in the ocean based on the quantitative association of POC with ballast minerals. *Deep Sea Res Part II Top Stud Oceanogr* **49**(1–3): 219–236. doi: 10.1016/S0967-0645(01)00101-1
- Arteaga LA, Pahlow M, Bushinsky SM, Sarmiento JL. 2019. Nutrient Controls on Export Production in the Southern Ocean. *Glob Biogeochem Cycles* **33**(8): 942–956. doi: 10.1029/2019GB006236
- Assmy P, Henjes J, Klaas C, Smetacek V. 2007. Mechanisms determining species dominance in a

phytoplankton bloom induced by the iron fertilization experiment EisenEx in the Southern Ocean. *Deep Sea Res Part Oceanogr Res Pap* **54**(3): 340–362. doi: 10.1016/j.dsr.2006.12.005

Assmy P, Smetacek V, Montresor M, Klaas C, Henjes J, Strass VH, Arrieta JM, Bathmann U, Berg GM, Breitbarth E, et al. 2013. Thick-shelled, grazer-protected diatoms decouple ocean carbon and silicon cycles in the iron-limited Antarctic Circumpolar Current. *Proc Natl Acad Sci* **110**(51): 20633–20638. doi: 10.1073/pnas.1309345110

Baines SB, Twining BS, Brzezinski MA, Nelson DM, Fisher NS. 2010. Causes and biogeochemical implications of regional differences in silicification of marine diatoms. *Glob Biogeochem Cycles* **24**(4). doi: 10.1029/2010GB003856

Baines SB, Twining BS, Vogt S, Balch WM, Fisher NS, Nelson DM. 2011. Elemental composition of equatorial Pacific diatoms exposed to additions of silicic acid and iron. *Deep Sea Res Part II Top Stud Oceanogr* **58**(3–4): 512–523. doi: 10.1016/j.dsr2.2010.08.003

van Beek P, Bourquin M, Reyss J-L, Souhaut M, Charette MA, Jeandel C. 2008. Radium isotopes to investigate the water mass pathways on the Kerguelen Plateau (Southern Ocean). *Deep Sea Res Part II Top Stud Oceanogr* **55**(5–7): 622–637. doi: 10.1016/j.dsr2.2007.12.025

Blain S, Capparos J, Guéneuguès A, Obernosterer I, Oriol L. 2015. Distributions and stoichiometry of dissolved nitrogen and phosphorus in the iron-fertilized region near Kerguelen (Southern Ocean). *Biogeosciences* **12**(2): 623–635. doi: 10.5194/bg-12-623-2015

Blain S, Quéguiner B, Armand L, Belviso S, Bombled B, Bopp L, Bowie A, Brunet C, Brussaard C, Carlotti F, et al. 2007. Effect of natural iron fertilization on carbon sequestration in the Southern Ocean. *Nature* **446**(7139): 1070–1074. doi: 10.1038/nature05700

Boyd PW. 2002. Environmental factors controlling phytoplankton processes in the Southern Ocean. *J Phycol* **38**(5): 844–861. doi: 10.1046/j.1529-8817.2002.t01-1-01203.x

de Boyer Montégut C, Madec G, Fischer A, Lazar A, Iudicone D. 2004. Mixed layer depth over the global ocean: An examination of profile data and a profile-based climatology. *J Geophys Res Oceans* **109**(C12). doi: 10.1029/2004JC002378

Brzezinski MA, Olson R, Chisholm S. 1990. Silicon availability and cell-cycle progression in marine diatoms. *Mar Ecol Prog Ser* **67**: 83–96. doi: 10.3354/meps067083

Brzezinski MA. 1985. The Si:C:N ratio of marine diatoms: interspecific variability and the effect of some environmental variables. *J Phycol* **21**(3): 347–357. doi: 10.1111/j.0022-3646.1985.00347.x

Brzezinski MA, Baines SB, Balch WM, Beucher CP, Chai F, Dugdale RC, Krause JW, Landry MR, Marchi A, Measures CI, et al. 2011. Co-limitation of diatoms by iron and silicic acid in the equatorial Pacific. *Deep Sea Res Part II Top Stud Oceanogr* **58**(3–4): 493–511. doi: 10.1016/j.dsr2.2010.08.005

Buesseler KO. 1998. The decoupling of production and particulate export in the surface ocean. *Glob Biogeochem Cycles* **12**(2): 297–310. doi: 10.1029/97GB03366

Burd AB, Jackson GA. 2009. Particle Aggregation. *Annu Rev Mar Sci* **1**(1): 65–90. doi: 10.1146/annurev.marine.010908.163904

Closset I, Lasbleiz M, Leblanc K, Quéguiner B, Cavaña A-J, Elskens M, Navez J, Cardinal D. 2014. Seasonal evolution of net and regenerated silicon production around a natural Fe-fertilized area in the Southern Ocean estimated with Si isotopic approaches. **11**(20): 5827–5846. doi: 10.5194/bg-11-5827-2014

Cornet-Barthaux V, Armand L, Quéguiner B. 2007. Biovolume and biomass estimates of key diatoms in the Southern Ocean. *Aquat Microb Ecol* **48**: 295–308. doi: 10.3354/ame048295

Crombet Y, Leblanc K, Quéguiner B, Moutin T, Rimmelin P, Ras J, Claustre H, Leblond N, Oriol L, Pujo-Pay M. 2011. Deep silicon maxima in the stratified oligotrophic Mediterranean Sea. *Biogeosciences* **8**(2): 459–475. doi: 10.5194/bg-8-459-2011

Doucette GJ, Fryxell GA. 1983. *Thalassiosira antarctica*: vegetative and resting stage chemical composition of an ice-related marine diatom. *Mar Biol* **78**(1): 1–6. doi: 10.1007/BF00392964

Dugdale RC, Wilkerson FP, Minas HJ. 1995. The role of a silicate pump in driving new production. *Deep Sea Res Part Oceanogr Res Pap* **42**(5): 697–719. doi: 10.1016/0967-0637(95)00015-X

Durkin CA, Marchetti A, Bender S, Truong T, Morales R, Mock T, Armbrust E. 2012. Frustule-related

gene transcription and the influence of diatom community composition on silica precipitation in an iron-limited environment. *Limnol Ocean* **57**(6): 1619–1633. doi: 10.4319/lo.2012.57.6.1619

Durkin CA, Van Mooy BAS, Dyhrman ST, Buesseler KO. 2016. Sinking phytoplankton associated with carbon flux in the Atlantic Ocean: Sinking phytoplankton and carbon flux. *Limnol. Oceanogr.* **61**, 1172–1187. <https://doi.org/10.1002/lno.10253>

Franck VM, Brzezinski MA, Coale KH, Nelson DM. 2000. Iron and silicic acid concentrations regulate Si uptake north and south of the Polar Frontal Zone in the Pacific Sector of the Southern Ocean. *Deep Sea Res Part II Top Stud Oceanogr* **47**: 3315–3338.

Frölicher TL, Sarmiento JL, Paynter DJ, Dunne JP, Krasting JP, Winton M. 2015. Dominance of the Southern Ocean in Anthropogenic Carbon and Heat Uptake in CMIP5 Models. *J Clim* **28**(2): 862–886. doi: 10.1175/JCLI-D-14-00117.1

González H. 1992. Distribution and abundance of micropellets around the Antarctic peninsula. Implications for protistan feeding behaviour. *Mar Ecol Prog Ser* **90**: 223–236. doi: 10.3354/meps090223

Hamm CE, Merkel R, Springer O, Jurkojc P, Maier C, Prectel K, Smetacek V. 2003. Architecture and material properties of diatom shells provide effective mechanical protection. *Nature* **421**(6925): 841–843. doi: 10.1038/nature01416

Henson, S., Le Moigne, F., Giering, S., 2019. Drivers of Carbon Export Efficiency in the Global Ocean. *Glob. Biogeochem. Cycles* **33**, 891–903. <https://doi.org/10.1029/2018GB006158>

Hoban MA, Fryxell GA, Buck KR. 1980. Biddulphioid diatoms: Resting spores in antarctic Eucampia and Odontella. *J Phycol* **16**(4): 591–602. doi: 10.1111/j.1529-8817.1980.tb03078.x

Hoffmann LJ, Peeken I, Lochte K. 2007. Effects of iron on the elemental stoichiometry during EIFEX and in the diatoms *Fragilariopsis kerguelensis* and *Chaetoceros dichaeta*. *Biogeosciences* **4**(4): 569–579.

Hoffmann LJ, Peeken I, Lochte K, Assmy P, Veldhuis M. 2006. Different reactions of Southern Ocean

phytoplankton size classes to iron fertilization. *Limnol Oceanogr* **51**(3): 1217–1229. doi: 10.4319/lo.2006.51.3.1217

Hutchins DA, Bruland KW. 1998. Iron-limited diatom growth and Si:N uptake ratios in a coastal upwelling regime. *Nature* **393**(6685): 561–564. doi: 10.1038/31203

Jackson GA, Waite AM, Boyd PW. 2005. Role of algal aggregation in vertical carbon export during SOIREE and in other low biomass environments. *Geophys Res Lett* **32**(13). doi: 10.1029/2005GL023180

Jacques G. 1983. Some ecophysiological aspects of the Antarctic phytoplankton. *Polar Biol* **2**(1): 27–33. doi: 10.1007/BF00258282

Jeandel C, Ruiz-Pino D, Gjata E, Poisson A, Brunet C, Charriauc E, Dehairs F, Delille D, Fiala M, Fravallo C, et al. 1998. KERFIX, a time-series station in the Southern Ocean: a presentation. *J Mar Syst* **17**(1–4): 555–569. doi: 10.1016/S0924-7963(98)00064-5

Kagami M, de Bruin A, Ibelings BW, Van Donk E. 2007. Parasitic chytrids: their effects on phytoplankton communities and food-web dynamics. *Hydrobiologia* **578**(1): 113–129. doi: 10.1007/s10750-006-0438-z

Kemp A, Villareal T. 2013. High diatom production and export in stratified waters – A potential negative feedback to global warming. *Prog Ocean* **119**: 4–23. doi: 10.1016/j.pocean.2013.06.004

Kopczyńska EE, Fiala M, Jeandel C. 1998. Annual and interannual variability in phytoplankton at a permanent station off Kerguelen Islands, Southern Ocean. *Polar Biol* **20**(5): 342–351. doi: 10.1007/s003000050312

Kopczynska EE, Weber LH, El-Sayed SZ. 1986. Phytoplankton species composition and abundance in the Indian sector of the Antarctic Ocean. *Polar Biol* **6**(3): 161–169. doi: 10.1007/BF00274879

Korb R, Whitehouse M, Atkinson A, Thorpe S. 2008. Magnitude and maintenance of the phytoplankton bloom at South Georgia: a naturally iron-replete environment. *Mar Ecol Prog Ser* **368**: 75–91. doi: 10.3354/meps07525

Korb R, Whitehouse M. 2004. Contrasting primary production regimes around South Georgia, Southern Ocean: large blooms versus high nutrient, low chlorophyll waters. *Deep Sea Res Part Oceanogr Res Pap* **51**(5): 721–738. doi: 10.1016/j.dsr.2004.02.006

Kranzler CF, Krause JW, Brzezinski MA, Edwards BR, Biggs WP, Maniscalco M, McCrow JP, Van Mooy BAS, Bidle KD, Allen AE, et al. 2019. Silicon limitation facilitates virus infection and mortality of marine diatoms. *Nat Microbiol*, in press. doi: 10.1038/s41564-019-0502-x

Kuwata A, Hama T, Takahashi M. 1993. Ecophysiological characterization of two life forms, resting spores and resting cells, of a marine planktonic diatom, *Chaetoceros pseudocurvisetus*, formed under nutrient depletion. *Mar Ecol Prog Ser* **102**(3): 245–255.

Kuwata A, Takahashi M. 1990. Life-form population responses of a marine planktonic diatom, *Chaetoceros pseudocurvisetus*, to oligotrophication in regionally upwelled water. *Mar Biol* **107**(3): 503–512. doi: 10.1007/BF01313435

Kuwata A, Takahashi M. 1999. Survival and recovery of resting spores and resting cells of the marine planktonic diatom *Chaetoceros pseudocurvisetus* under fluctuating nitrate conditions. *Mar Biol* **134**(3): 471–478. doi: 10.1007/s002270050553

Kuwata A, Tsuda A. 2005. Selection and viability after ingestion of vegetative cells, resting spores and resting cells of the marine diatom, *Chaetoceros pseudocurvisetus*, by two copepods. *J Exp Mar Biol Ecol* **322**(2): 143–151. doi: 10.1016/j.jembe.2005.02.013

Lam P, Bishop J. 2007. High biomass, low export regimes in the Southern Ocean. *Deep Sea Res Part II Top Stud Ocean* **54**(5–7): 601–638. doi: 10.1016/j.dsr2.2007.01.013

Lasbleiz M, Leblanc K, Armand L, Christaki U, Georges C, Obernosterer I, Quéguiner B. 2016. Composition of diatom communities and their contribution to plankton biomass in the naturally iron-fertilized region of Kerguelen in the Southern Ocean. *Fems Microbiol Ecol* **92**(11): fiw171. doi: 10.1093/femsec/fiw171

Lasbleiz M, Leblanc K, Blain S, Ras J, V C-B, Nunige S, Quéguiner B. 2014. Pigments, elemental composition (C, N, P, and Si), and stoichiometry of particulate matter in the naturally iron fertilized region of Kerguelen in the Southern Ocean. *Biogeosciences* **11**(20): 5931–5955. doi: 10.5194/bg-11-

5931-2014

Leblanc K, Arístegui J, Armand L, Assmy P, Beker B, Bode A, Breton E, Cornet V, Gibson J, Gosselin M-P, et al. 2012. A global diatom database – abundance, biovolume and biomass in the world ocean. *Earth Syst Sci Data* **4**(1): 149–165. doi: 10.5194/essd-4-149-2012

Leblanc K, Hare CE, Boyd PW, Bruland KW, Sohst B, Pickmere S, Lohan MC, Buck K, Ellwood M, Hutchins DA. 2005. Fe and Zn effects on the Si cycle and diatom community structure in two contrasting high and low-silicate HNLC areas. *Deep Sea Res Part Oceanogr Res Pap* **52**(10): 1842–1864. doi: 10.1016/j.dsr.2005.06.005

Leblanc K, Hutchins DA. 2005. New applications of a biogenic silica deposition fluorophore in the study of oceanic diatoms. *Limnol Oceanogr Methods* **3**(10): 462–476. doi: 10.4319/lom.2005.3.462

Legendre P, Legendre L. 2012. *Numerical Ecology*. 3. Eng. ed. Amsterdam: Elsevier. (Developments in environmental modelling; Vol. 24).

Lomas MW, Baer SE, Acton S, Krause JW. 2019. Pumped Up by the Cold: Elemental Quotas and Stoichiometry of Cold-Water Diatoms. *Front. Mar Sci* **6**. doi: 10.3389/fmars.2019.00286

Maiti K, Charette MA, Buesseler KC, Kahru M. 2013. An inverse relationship between production and export efficiency in the Southern Ocean. *Geophys Res Lett* **40**(8): 1557–1561. doi: 10.1002/grl.50219

Marchetti A, Cassar N. 2009. Diatom elemental and morphological changes in response to iron limitation: a brief review with potential paleoceanographic applications. *Geobiology* **7**(4): 419–431. doi: 10.1111/j.1472-4669.2009.00207.x

Martin J. 1990. Glacial-interglacial CO₂ change: The Iron Hypothesis. *Paleoceanography* **5**(1): 1–13. doi: 10.1029/PA005i001p00001

McNair HM, Brzezinski MA, Krause JW. 2015. Quantifying diatom silicification with the fluorescent dye, PDMPD. *Limnol Oceanogr Methods* **13**(10): 587–599. doi: 10.1002/lom3.10049

McNair HM, Brzezinski MA, Krause JW. 2018. Diatom populations in an upwelling environment decrease silica content to avoid growth limitation. *Environ Microbiol* **20**(11): 4184–4193. doi:

10.1111/1462-2920.14431

McQuoid MR, Hobson LA. 1996. Diatom resting stages. *J Phycol* **32**(6): 889–902. doi: 10.1111/j.0022-3646.1996.00889.x

Mongin M, Molina E, Trull TW. 2008. Seasonality and scale of the Kerguelen plateau phytoplankton bloom: A remote sensing and modeling analysis of the influence of natural iron fertilization in the Southern Ocean. *Deep Sea Res Part II Top Stud Oceanogr* **55**(5–7): 880–892. doi: 10.1016/j.dsr2.2007.12.039

Morris PJ, Sanders R, Turnewitsch R, Thomalla S. 2007. ²³⁴Th-derived particulate organic carbon export from an island-induced phytoplankton bloom in the Southern Ocean. *Deep Sea Res Part II Top Stud Oceanogr* **54**(18–20): 2208–2232. doi: 10.1016/j.dsr2.2007.06.002

Mosseri J, Quéguiner B, Armand L, Cornet-Barthaux V. 2008. Impact of iron on silicon utilization by diatoms in the Southern Ocean: A case study of Si₄ cycle decoupling in a naturally iron-enriched area. *Deep Sea Res Part II Top Stud Oceanogr* **55**(5–7): 801–819. doi: 10.1016/j.dsr2.2007.12.003

Nelson DM, Brzezinski MA, Sigmon DE, Franck VM. 2001. A seasonal progression of Si limitation in the Pacific sector of the Southern Ocean. *Deep Sea Res Part II Top Stud Oceanogr* **48**(19–20): 3973–3995. doi: 10.1016/S0967-0645(01)00076-5

Nelson DM, Tréguer P. 1992. Role of silicon as a limiting nutrient to Antarctic diatoms: evidence from kinetic studies in the Ross Sea ice-edge zone. *Mar Ecol Prog Ser* **80**(2/3): 255–264.

Oku O, Kamatani A. 1995. Resting spore formation and phosphorus composition of the marine diatom *Chaetoceros pseudocurvisetus* under various nutrient conditions. *Mar Biol* **123**(2): 393–399. doi: 10.1007/BF00353630

Paasche E. 1973. Silicon and the ecology of marine plankton diatoms. I. *Thalassiosira pseudonana* (*Cyclotella nana*) grown in a chemostat with silicate as limiting nutrient. *Mar Biol* **19**(2): 117–126. doi: 10.1007/BF00353582

Park Y-H, Durand I, Kestenare E, Rougier G, Zhou M, d'Ovidio F, Cotté C, Lee J. 2014. Polar Front around the Kerguelen Islands: An up-to-date determination and associated circulation of

surface/subsurface waters. *J Geophys Res Oceans* **119**(10): 6575–6592. doi: 10.1002/2014JC010061

Park Y-H, Fuda J-L, Durand I, Naveira Garabato AC. 2008a. Internal tides and vertical mixing over the Kerguelen Plateau. *Deep Sea Res Part II Top Stud Oceanogr* **55**(5–7): 582–593. doi: 10.1016/j.dsr2.2007.12.027

Park Y-H, Roquet F, Durand I, Fuda J-L. 2008b. Large-scale circulation over and around the Northern Kerguelen Plateau. *Deep Sea Res Part II Top Stud Oceanogr* **55**(5–7): 566–581. doi: 10.1016/j.dsr2.2007.12.030

Pauthenet E, Roquet F, Madec G, Guinet C, Hindell M, McMahon C, Harcourt R, Nerini D. 2018. Seasonal Meandering of the Polar Front Upstream of the Kerguelen Plateau. *Geophys Res Lett* **45**(18): 9774–9781. doi: 10.1029/2018GL079614

Pelusi A, Margiotta F, Passarelli A, Ferrante MI, Ribera d'Alicà M, Montresor M. 2020 May 27. Density-dependent mechanisms regulate spore formation in the diatom *Chaetoceros socialis*. *Limnol Oceanogr Lett*, in press. doi: 10.1002/lol2.10159

Planchon F, Ballas D, Cavagna A-J, Bowie AR, Davies D, Trull T, Laurenceau-Cornec EC, Van Der Merwe P, Dehairs F. 2015. Carbon export in the naturally iron-fertilized Kerguelen area of the Southern Ocean based on the ^{234}Th approach. *Biogeosciences* **12**(12): 3831–3848. doi: 10.5194/bg-12-3831-2015

Pollard R, Salter I, Sanders P, Lucas M, Moore C, Mills R, Statham P, Allen J, Baker A, Bakker D, et al. 2009. Southern Ocean deep-water carbon export enhanced by natural iron fertilization. *Nature* **457**(7229): 577–580. doi: 10.1038/nature07716

Quéguiner B. 2001. Biogenic silica production in the Australian sector of the Subantarctic Zone of the Southern Ocean in late summer 1998. *J Geophys Res Oceans* **106**(C12): 31627–31636. doi: 10.1029/2000JC000249

Quéguiner B. 2013. Iron fertilization and the structure of planktonic communities in high nutrient regions of the Southern Ocean. *Deep Sea Res Part II Top Stud Oceanogr* **90**: 43–54. doi: 10.1016/j.dsr2.2012.07.024

Quéguiner B, Brzezinski MA. 2002. Biogenic silica production rates and particulate organic matter distribution in the Atlantic sector of the Southern Ocean during austral spring 1992. *Deep Sea Res Part II Top Stud Oceanogr* **49**(9–10): 1765–1786. doi: 10.1016/S0967-0645(02)00011-5

Quéguiner B, Treguer P, Peeken I, Scharek R. 1997. Biogeochemical dynamics and the silicon cycle in the Atlantic sector of the Southern Ocean during austral spring 1992. *Deep Sea Res Part II Top Stud Oceanogr* **44**(1–2): 69–89.

Ragueneau O, Savoye N, Amo Y, Cotten J, Tardiveau B, Leynaert A. 2005. A new method for the measurement of biogenic silica in suspended matter of coastal waters: using Si:Al ratios to correct for the mineral interference. *25*(5–6): 697–710. doi: 10.1016/j.csr.2004.05.017

Ragueneau O, Tréguer P. 1994. Determination of biogenic silica in coastal waters: applicability and limits of the alkaline digestion method. *Mar Chem* **45**(1–2): 43–51. doi: 10.1016/0304-4203(94)90090-6

Ras J, Claustre H, Uitz J. 2008. Spatial variability of phytoplankton pigment distributions in the Subtropical South Pacific Ocean: comparison between in situ and predicted data. *Biogeosciences* **5**(2): 353–369. doi: 10.5194/bg-5-353-2008

Redfield AC. 1958. The biological control of chemical factors in the environment. *Am Sci* **46**(3): 205–221.

Redfield AC, Ketchum DH, Richards FA. 1963. The influence of organisms on the composition of seawater. *The Sea*: 26–77. New York.

Rembauville M, Salter I, Leblond N, Gueneugues A, Blain S. 2015a. Export fluxes in a naturally iron-fertilized area of the Southern Ocean – Part 1: Seasonal dynamics of particulate organic carbon export from a moored sediment trap. *Biogeosciences* **12**(11): 3153–3170. doi: 10.5194/bg-12-3153-2015

Rembauville M, Blain S, Armand L, Quéguiner B, Salter I. 2015b. Export fluxes in a naturally iron-fertilized area of the Southern Ocean – Part 2: Importance of diatom resting spores and faecal pellets for export. *Biogeosciences* **12**(11): 3171–3195. doi: 10.5194/bg-12-3171-2015

Rembauville M, Blain S, Caparros J, Salter I. 2016. Particulate matter stoichiometry driven by microplankton community structure in summer in the Indian sector of the Southern Ocean. *Limnol Ocean* **61**(4): 1301–1321. doi: 10.1002/lno.10291

Rembauville M, Blain S, Manno C, Tarling G, Thompson A, Wolff G, Salter I. 2018. The role of diatom resting spores in pelagic–benthic coupling in the Southern Ocean. *Biogeosciences* **15**(10): 3071–3084. doi: 10.5194/bg-15-3071-2018

Rembauville M, Manno C, Tarling GA, Blain S, Salter I. 2016. Strong contribution of diatom resting spores to deep-sea carbon transfer in naturally iron-fertilized water downstream of South Georgia. *Deep Sea Res Part Ocean Res Pap* **115**: 22–35. doi: 10.1016/j.dsr.2016.05.002

Sackett O, Armand L, Beardall J, Hill R, Doblin M, Connelly C, Howes J, Stuart B, Ralph P, Heraud P. 2014. Taxon-specific responses of Southern Ocean diatoms to Fe enrichment revealed by synchrotron radiation FTIR microspectroscopy. *Biogeosciences* **11**(20): 5795–5808. doi: 10.5194/bg-11-5795-2014

Sallée J-B, Matear RJ, Rintoul SR, Lenton A. 2012. Localized subduction of anthropogenic carbon dioxide in the Southern Hemisphere oceans. *Nat Geosci* **5**(8): 579–584. doi: 10.1038/ngeo1523

Salter I, Kemp AE, Moore MC, Lampitt RS, Wolff GA, Holtvoeth J. 2012. Diatom resting spore ecology drives enhanced carbon export from a naturally iron-fertilized bloom in the Southern Ocean. *Global Biogeochem Cycles* **26**, GB1014, doi:10.1029/2010GB003977.

Sarmiento JL, Gruber N, Brzezinski M, Dunne J. 2004. High-latitude controls of thermocline nutrients and low latitude biological productivity. *Nature* **427**, 56–60. doi: 10.1038/nature02127

Sassenhagen, I., Irion, S., Jardillier, L., Moreira, D., Christaki, U., 2020. Protist Interactions and Community Structure During Early Autumn in the Kerguelen Region (Southern Ocean). *Protist* **171**, 125709. <https://doi.org/10.1016/j.protis.2019.125709>

Savoye N, Trull TW, Jacquet SHM, Navez J, Dehairs F. 2008. ²³⁴Th-based export fluxes during a natural iron fertilization experiment in the Southern Ocean (KEOPS). *Deep Sea Res Part II Top Stud Ocean* **55**(5–7): 841–855. doi: 10.1016/j.dsr2.2007.12.036

Sherr E, Sherr B. 2007. Heterotrophic dinoflagellates: a significant component of microzooplankton biomass and major grazers of diatoms in the sea. *Mar Ecol Prog Ser* **352**: 187–197. doi: 10.3354/meps07161

Smayda TJ. 1978. From phytoplankton to biomass. In: Sournia A, editor. Monographs on oceanographic methodology 6. Phytoplankton manual. UNESCO, Paris, p 273–279.

Smetacek V, Assmy P, Henjes J. 2004. The role of grazing in structuring Southern Ocean pelagic ecosystems and biogeochemical cycles. *Antarct Sci* **16**(4): 541–558. doi: 10.1017/S0954102004002317

Sugie K, Kuma K. 2008. Resting spore formation in the marine diatom *Thalassiosira nordenskioeldii* under iron- and nitrogen-limited conditions. *J Plankton Res* **30**(11): 1245–1255. doi: 10.1093/plankt/fbn080

Takahashi T, Sweeney C, Hales B, Chipman D, Newberger T, Goddard J, Iannuzzi R, Sutherland S. 2012. The Changing Carbon Cycle in the Southern Ocean. *Oceanography* **25**(3): 26–37. doi: 10.5670/oceanog.2012.71

Takeda S. 1998. Influence of iron availability on nutrient consumption ratio of diatoms in oceanic waters. *Nature* **393**(6687): 774–777. doi: 10.1038/31674

Tréguer P, Bowler C, Moriceau C, Dutkiewicz S, Gehlen M, Aumont O, Bittner L, Dugdale R, Finkel Z, Iudicone D, et al. 2013. Influence of diatom diversity on the ocean biological carbon pump. *Nat Geosci* **11**(1): 27–37. doi: 10.1038/s41561-017-0028-x

Twining BS, Baines SB, Fisher NS. 2004. Element stoichiometries of individual plankton cells collected during the Southern Ocean Iron Experiment (SOFEX). *Limnol Oceanogr* **49**(6): 2115–2128. doi: 10.4319/lo.2004.49.6.2115

Uitz J, Claustre H, Griffiths F, Ras J, Garcia N, Sandroni V. 2009. A phytoplankton class-specific primary production model applied to the Kerguelen Islands region (Southern Ocean). *Deep Sea Res Part Ocean Res Pap* **56**(4): 541–560. doi: 10.1016/j.dsr.2008.11.006

Utermöhl H. 1931. Neue Wege in der quantitativen Erfassung des Plankton.(Mit besonderer

Berücksichtigung des Ultraplanktons.): Mit 4 Abbildungen im Text. *SIL Proc 1922-2010* **5**(2): 567–596. doi: 10.1080/03680770.1931.11898492

Whitehouse MJ, Priddle J, Symon C. 1996. Seasonal and annual change in seawater temperature, salinity, nutrient and chlorophyll a distributions around South Georgia, South Atlantic. *Deep Sea Res Part Oceanogr Res Pap* **43**(4): 425–443. doi: 10.1016/0967-0637(96)00020-9

Wilken S, Hoffmann B, Hersch N, Kirchgessner N, Dieluweit S, Rubner W, Hoffmann LJ, Merkel R, Peeken I. 2011. Diatom frustules show increased mechanical strength and altered valve morphology under iron limitation. *Limnol Oceanogr* **56**(4): 1399–1410. doi: 10.4319/lo.2011.56.4.1399

Zhou M, Zhu Y, d'Ovidio F, Park Y-H, Durand I, Kestenare E, Sarria V, Van-Beek P, Quéguiner B, Carlotti F, et al. 2014. Surface currents and upwelling in Kerguelen Plateau regions. *Biogeosciences Discuss* **11**(5): 6845–6876. doi: 10.5194/bgd-11-6845-2014

The structure of diatom communities constrains biogeochemical properties in surface waters of the Southern Ocean (Kerguelen Plateau)

Augustin Lafond¹, Karine Leblanc¹, Justine Legras¹, Véronique Cornet¹, Bernard Quéguiner¹

¹Aix-Marseille University, Université de Toulon, CNRS, IRD, MIO, UM 110, 13288, Campus de Luminy, 163 avenue de Luminy, 13288 Marseille, France

Correspondence: augustin.lafond@gmail.com

Supplementary material

Table S1. Range and mean (in parentheses when given together) values of linear measurements, biovolume, and carbon biomass of major diatom taxa observed during MOBYDICK. N = number of observations; D = diameter; AA = apical axis; TA = transapical axis; PA = pervalvar axis; CV = coefficient of variation. Shapes were used to estimate volume from linear dimensions: RB = rectangular box; C = cylinder; EC = elliptic cylinder; EC + 4H = elliptic cylinder + 4 horns; S = spindle; CU = cuboid; PP = prism on parallelogram base.

Species and genera groupings	N	D (μm)	AA (μm)	TA (μm)	PA (μm)	Shape	Biovolume (μm^3)	CV (%)	Cell carbon (pg cell ⁻¹)
<i>Actinocyclus octonarius</i>	32	41.4-122.7 (57.3)				C	91364	132	2619
<i>Actinocyclus / Thalassiosira spp.</i>	1332	7.1-49.6 (14.3)			4-23.4 (9.7)	C	2865	237	189
<i>Azpeitia tabularis</i>	25	34.4-82.1 (48.3)				C	69309	83	2123
<i>Chaetoceros atlanticum</i> (chain)	148		7.1-29.9 (17.4)		6.5-7.7 (7.1)	EC	2874	62	189
<i>Chaetoceros atlanticum</i> , (sigmoid)	942		7-31.5 (15.2)	7.5-12.2 (10.2)	4.1-35.2 (10.9)	EC	1489	67	115
<i>Chaetoceros atlanticum</i> (bulbosum)	234		8.3-24.1 (15.3)	9.8-19.2 (13.1)	6.8-19.3 (12)	EC	1933	51	140
<i>Chaetoceros castracanaei</i>	71		8.5-16.6 (12.8)	6.5-18.3 (13.6)	5.4-20.2 (11.6)	EC	1098	41	91
<i>Chaetoceros criophilus</i>	19		9.3-61.4 (16.2)		9.4-74.5 (16.9)	EC	10378	338	501
<i>Chaetoceros dichæta</i>	100		14.1-45.8 (23.5)		9.4-30.7 (15.6)	EC	4987	65	287
<i>Chaetoceros cf neglectus</i>	130		2.6-17.3 (5.8)		2.1-9.7 (4.4)	EC	92	98	14
<i>Chaetoceros resting spores</i>	100		4.2-14.7 (5.4)		3.3-7.4 (4.6)	EC	94	60	44
<i>Chaetoceros sp.</i> (small <i>Hyalochaete</i>)	93		5.4-18.3 (11.8)	4.8-8.9 (7)		EC	632	53	60
<i>Corethron inerme</i>	1571	12.9-43 (30.1)			33.3-197.4 (98.5)	C	62874	52	1972
<i>Corethron pennatum</i> (syn: <i>C. criophilum</i>)	67	6-75.9 (30.9)			16.4-434.5 (166.5)	C	316627	136	6736
<i>Dactyliosolen antarctica</i>	79	14.1-71.7 (37.2)			34.4-215.6 (119.1)	C	148697	67	3793
<i>Eucampia antarctica</i> (typical)	263		21.1-62.9 (51.2)	13.9-20.4 (17.3)	17.8-41 (29.2)	EC	20384	25	838
<i>Eucampia antarctica</i> (H shape)	216		15.6-52.8 (22.4)	14.4-19.3 (16.3)	16.8-51.7 (25.7)	EC + 4H	8702	73	439
<i>Guinardia cylindrus</i>	316	6.6-29.1 (15.9)			16.2-122.9 (54.7)	C	12429	76	575
<i>Leptocylindrus danicus</i>	51	5.1-13.9 (8.4)			24.8-160.8 (59.5)	C	4083	118	247
<i>Odontella weissflogii</i> resting cell	61		24.2-43 (31.8)		39.9-57.5 (48.2)	EC	25546	24	994
<i>Odontella weissflogii</i> resting spore	11		31.2-60.7 (52.8)		22.5-49 (45.2)	EC	75156	46	2258
<i>Proboscia alata</i>	181	8.9-45.8 (20.9)			238.3-1183 (644.6)	C	236232	67	5392
<i>Proboscia inermis</i> (winter form)	149	6.8-25.1 (11.2)			26-1070 (129)	C	18354	192	773
<i>Proboscia inermis</i>	56	8.4-35.7 (18.8)			180.6-909 (522.6)	C	189895	113	4567

<i>Rhizosolenia antennata/hebetata f. semispina</i>	25	7.8-38.3 (16.1)			221.7-1433.4 (749.7)	C	211809	165	4963
<i>Rhizosolenia chunii</i>	724	3.8-47.2 (16)			9.6-171.9 (34.8)	C	12393	175	574
<i>Rhizosolenia polydactyla f. polydactyla</i>	37	21.4-47.1 (38)			286.2-1433 (632.5)	C	754488	46	13032
<i>Thalassiosira lentiginosa</i>	69	38.4-90.2 (59.6)			4.8-10.5 (7.4)	C	25227	72	985
<i>Cylindrotheca closterium</i> (robust)	1027		5.7-41.7 (12.6)	0.9-6 (2.3)		S	200	158	25
<i>Cylindrotheca closterium</i> (thin)	302		4.6-12.9 (6.7)	1.4-7.3 (2.2)		S	44	60	8
<i>Fragilariopsis kerguelensis</i>	1300		10.8-92.9 (32.2)	6.3-15 (10.3)	3.7-15.3 (7.2)	EC	2111	78	149
<i>Fragilariopsis pseudonana</i>	417		1.5-13.5 (6.5)		1.4-9.4 (3)	EC	39	73	7
<i>Fragilariopsis rhombica</i>	68		10.4-35.5 (15.9)	6.3-12.2 (9.3)		EC	614	61	58
<i>Fragilariopsis rhombica/separanda</i>	44		15.7-44.6 (24)	6.3-17.4 (8.3)		EC	1227	102	99
<i>Membraneis</i> sp.	86		38.1-310.4 (110.4)	6.5-100.8 (36.6)		EC	87413	125	2533
<i>Pseudo-nitzschia cf lineola</i>	666		22.1-150.7 (88.7)	2.1-6.4 (3.8)	2.2-5 (3.9)	PP	481	38	49
<i>Pseudo-nitzschia cf heimii</i>	172		63.6-150.8 (90.2)	5-9 (6.7)	4.9-10 (6.4)	PP	1329	46	105
<i>Thalassionema nitzschioides</i>	1096		9.5-131.3 (26.2)	1.1-5.1 (4.1)	1.7-11.6 (4.2)	CU	695	217	64
<i>Thalassiothrix</i> sp.	19		744.4-1505.9 (110.8)	3.4-18.7 (9.8)		CU	139005	103	3603

Table S2. List of the taxa included in statistical analyses (i.e. hierarchical clustering and NMDS).

Diatom taxa	Reference
<i>Actinocyclus Thalassiosira</i> complex	Ehrenberg (1837) - Cleve (1873)
<i>Actinocyclus octonarius</i>	Ehrenberg (1837)
<i>Asteromphalus</i> spp.	Ehrenberg (1844)
<i>Azpeitia tabularis</i>	Fryxell and Sims (1986)
Centric	-
<i>Chaetoceros</i> spp.	Ehrenberg (1844)
<i>Chaetoceros atlanticus</i>	Cleve (1873)
<i>Chaetoceros castracanei</i>	Karsten (1905)
<i>Chaetoceros convolutus</i>	Castracane (1886)
<i>Chaetoceros criophylus</i>	Castracane (1886)
<i>Chaetoceros decipiens</i>	Cleve (1873)
<i>Chaetoceros dictyota</i>	Ehrenberg (1844)
<i>Chaetoceros neglectus</i>	Karsten (1905)
<i>Chaetoceros</i> spp. resting spore	-
<i>Corethron inerme</i>	Karsten (1905)
<i>Corethron pennatum</i>	(Grunow) Ostenfeld (1909)
<i>Coscinodiscus</i> spp.	Ehrenberg (1839)
<i>Coscinodiscus centralis</i>	Ehrenberg (1839)
<i>Cylindrotheca closterium</i>	(Ehrenberg) Reimann & J.C.Lewin (1964)
<i>Dactyliosolen antarcticus</i>	Castracane (1886)
<i>Dactyliosolen tenuijunctus</i>	(Manguin) Hasle (1975)
<i>Eucampia antarctica</i>	(Castracane) Mangin (1915)
<i>Fragilariopsis kerguelensis</i>	(O'Meara) Hustedt (1952)
<i>Fragilariopsis pseudonana</i>	(Hasle) Hasle (1993)
<i>Fragilariopsis rhombica</i>	(O'Meara) Hustedt (1952)
<i>Guinardia cylindrus</i>	(Cleve) Hasle (1996)
<i>Haslea trompii</i>	(Cleve) Simonsen (1974)
<i>Leptocylindrus danicus</i>	Cleve (1889)
<i>Leptocylindrus mediterraneus</i>	(H.Peragallo) Hasle (1975)
<i>Membraneis</i> spp.	Paddock (1988)
<i>Navicula</i> spp.	Bory (1822)
<i>Odontella weissflogii</i>	(Grunow) Grunow (1884)
<i>Plagiotropis</i> sp.	Pfitzer (1871)
<i>Pleurosigma</i> spp.	Smith (1852)
<i>Proboscia alata</i>	(Brightwell) Sundström (1986)

<i>Proboscia inermis</i>	(F.Castracane) R.W.Jordan & R.Ligowski (1991)
<i>Pseudo-nitzschia heimii</i>	Manguin (1957)
<i>Pseudo-nitzschia lineola</i>	(Cleve) Hasle (1993)
<i>Rhizosolenia</i> spp.	Brightwell (1858)
<i>Rhizosolenia antennata</i>	(Ehrenberg) N.E.Brown (1920)
<i>Rhizosolenia chunii</i>	Karsten (1905)
<i>Rhizosolenia curvata</i>	Zacharias (1905)
<i>Rhizosolenia polydactyla</i>	Castracane (1886)
<i>Rhizosolenia simplex</i>	Karsten (1905)
<i>Thalassionema nitzschioides</i>	(Grunow) Mereschkowsky (1902)
<i>Thalassiosira lentiginosa</i>	(Janisch) Fryxell (1977)
<i>Thalassiosira tumida</i>	(Janisch) Hasle (1971)
<i>Thalassiothrix antarctica</i>	Schimper and Karsten (1905)
Pennate	-

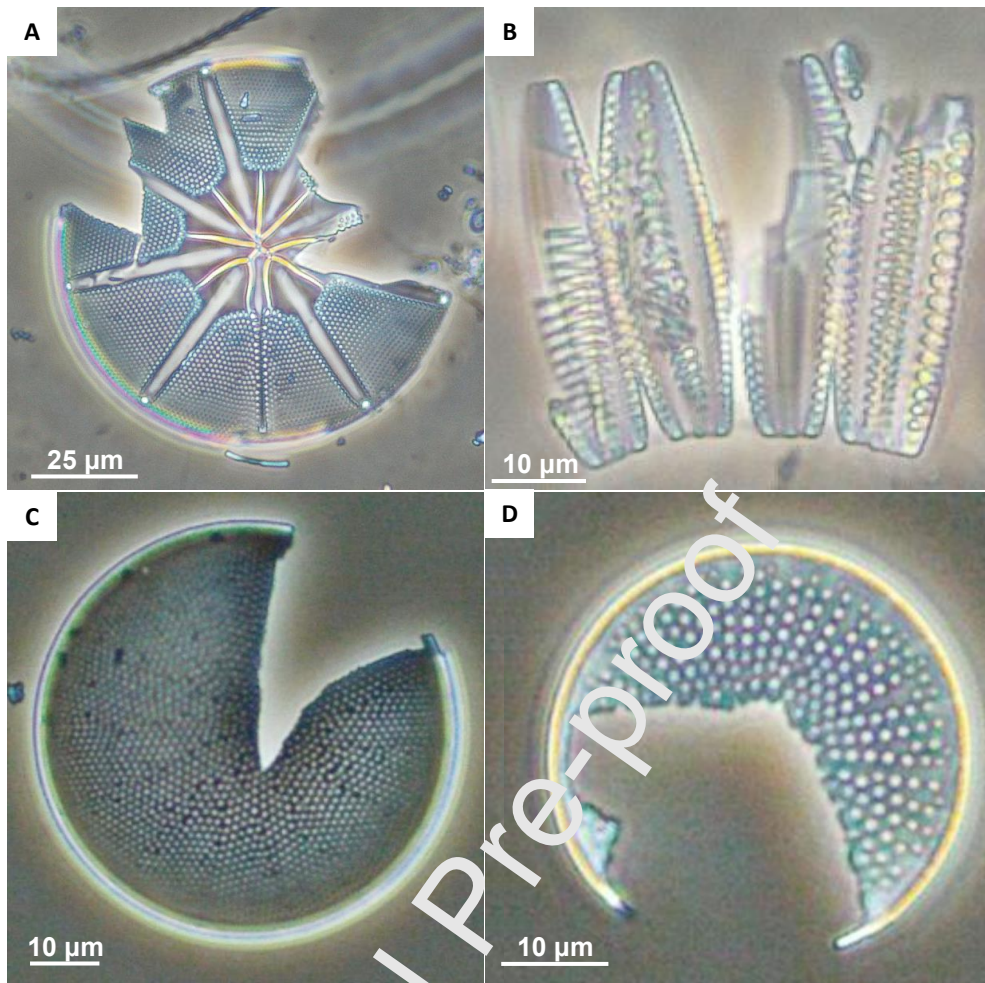


Figure S1. Selection of diatom images showing truncated frustules, which we considered as indicative of mesozooplankton grazing. (A) *Asteromphalus hookeri*, (B) *Fragilariopsis kerguelensis*, (C) *Thalassiosira lentiginosa*, (D) *Azpeitia tabularis*.

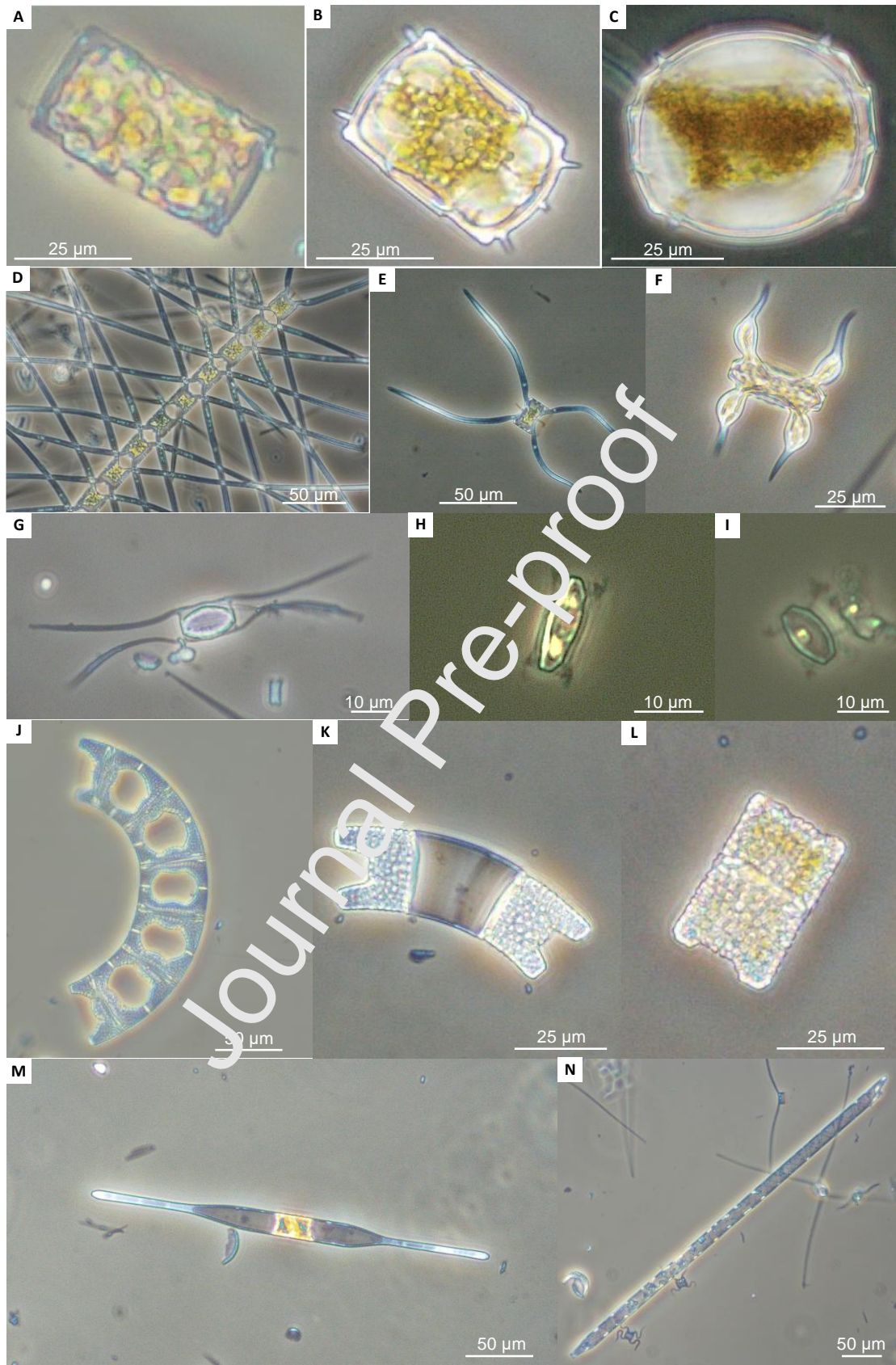


Figure S2. Selection of diatom images showing the variety of life stages and morphological forms within a same species. A) *Odontella weissflogii* vegetative cell, (B) *Odontella weissflogii* 'resting cell', (C) *Odontella weissflogii* 'resting spore', (D) *Chaetoceros atlanticum* 'colonial' form, (E) *Chaetoceros atlanticum* 'sigmoidal' form, (F) *Chaetoceros atlanticum* 'bulbosum' form, (G-I) *Chaetoceros* spp. resting spores, (J) *Eucampia antarctica* 'typical' form, (K) *Eucampia antarctica* 'H-shape' form, (L) *Eucampia antarctica* 'flat' form, (M) *Proboscia inerme* 'winter' form, (N) *Proboscia inerme* 'typical' form.

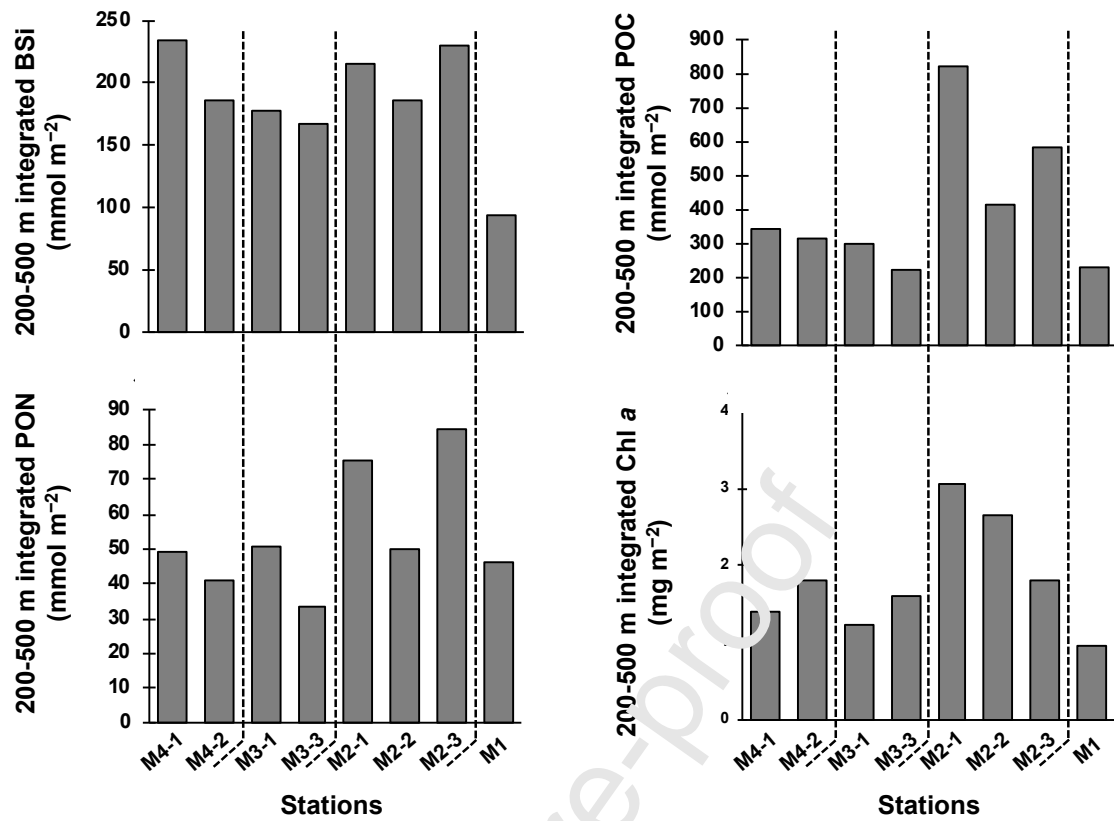


Figure S3. Integrated BSi, POC, PON, and Chl a concentration between 200 and 500 m at the four stations.

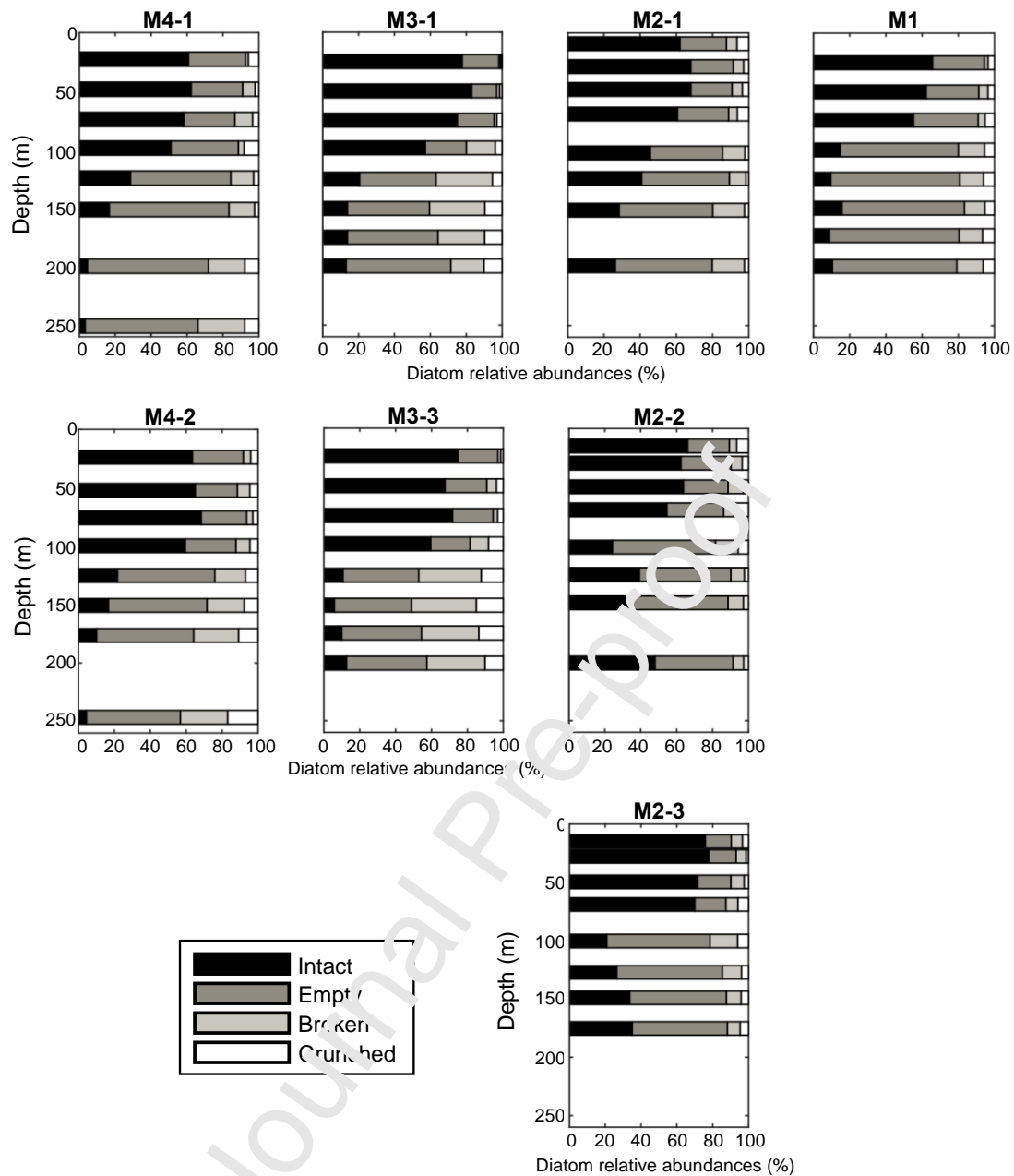


Figure S4. Diatom relative abundances (in percent) to intact, empty, broken and crunched frustule at the four stations.

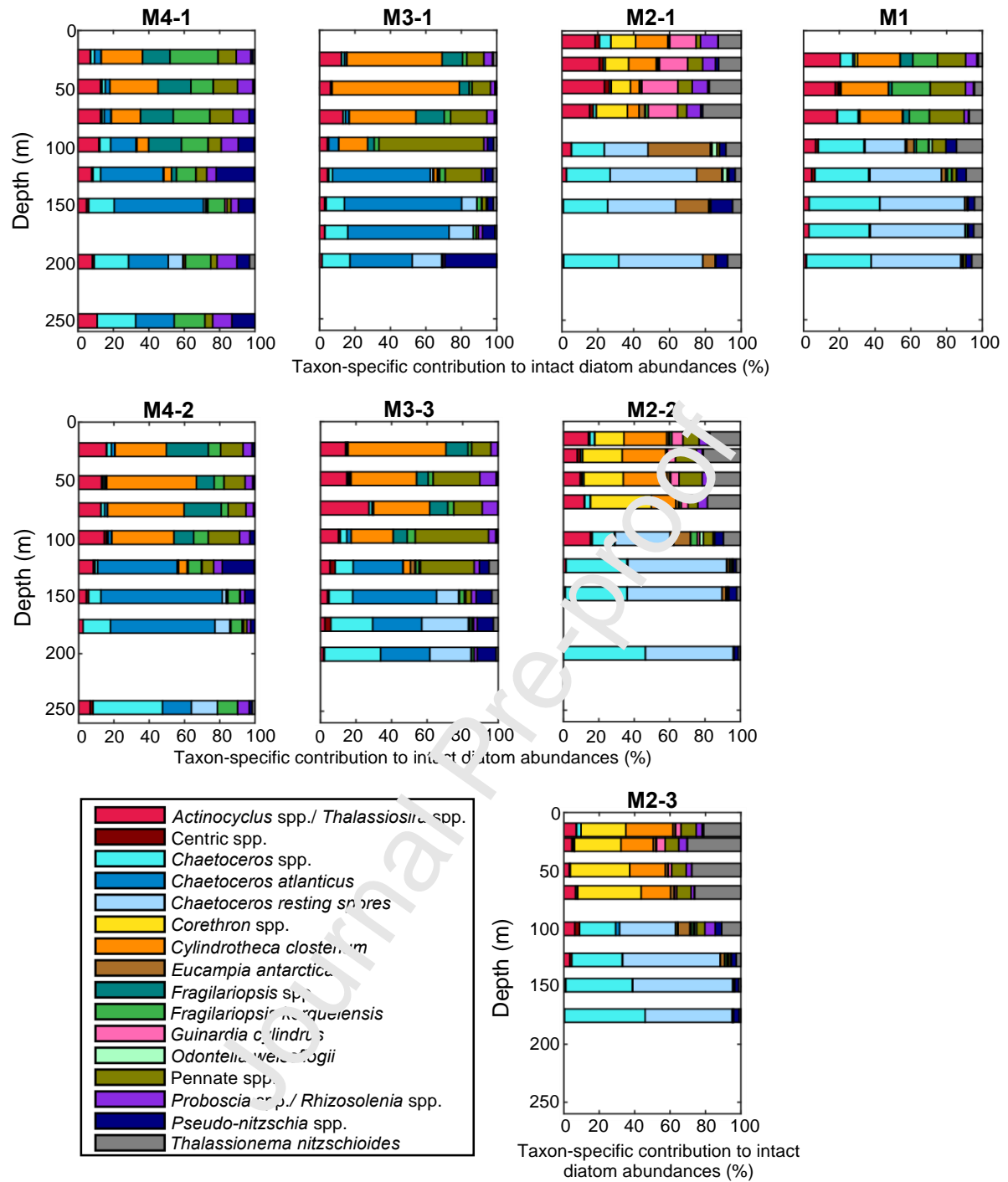


Figure S5. Taxon-specific contribution to intact diatom abundances at the four stations.

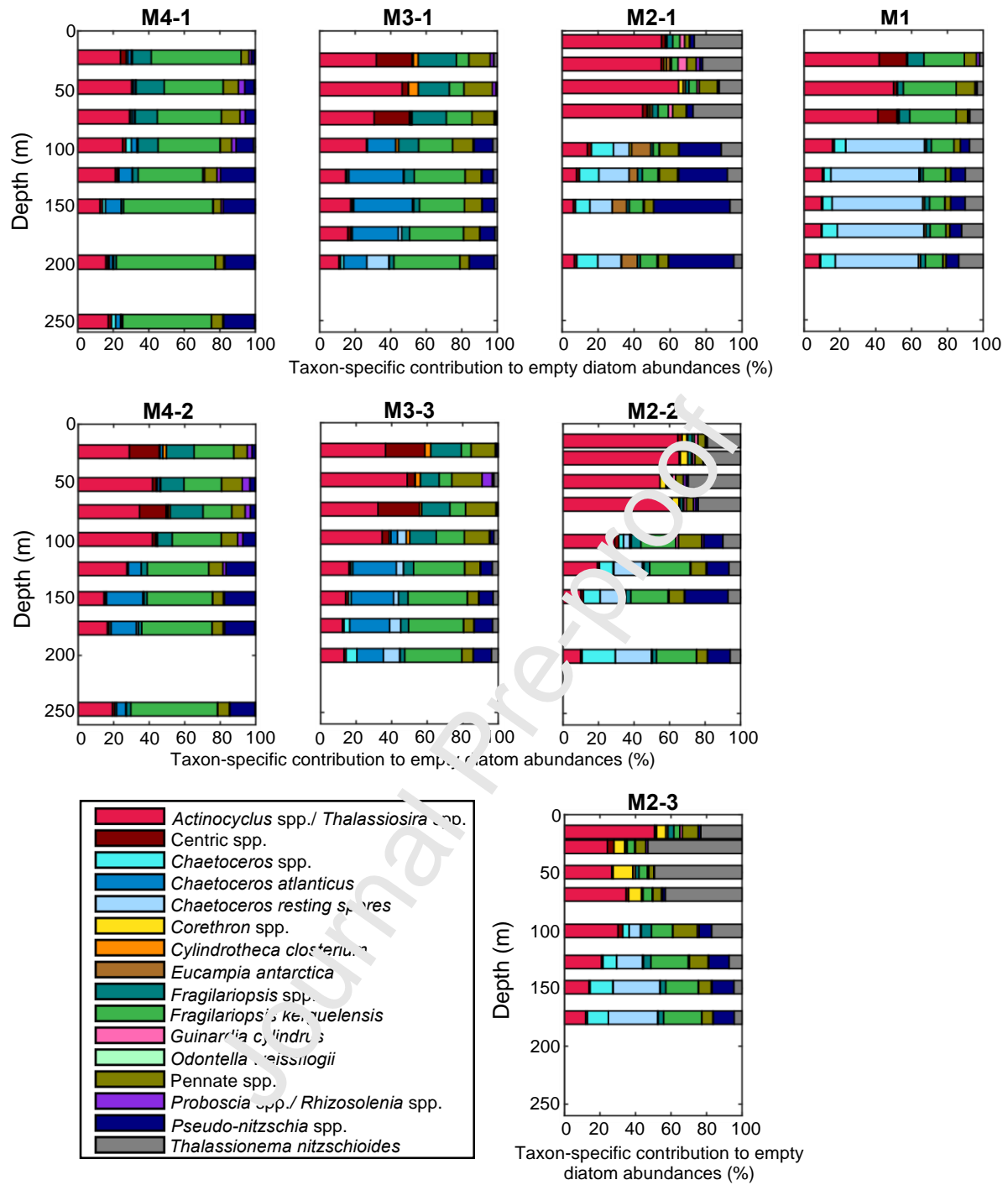


Figure S6. Taxon-specific contribution to empty diatom abundances at the four stations.

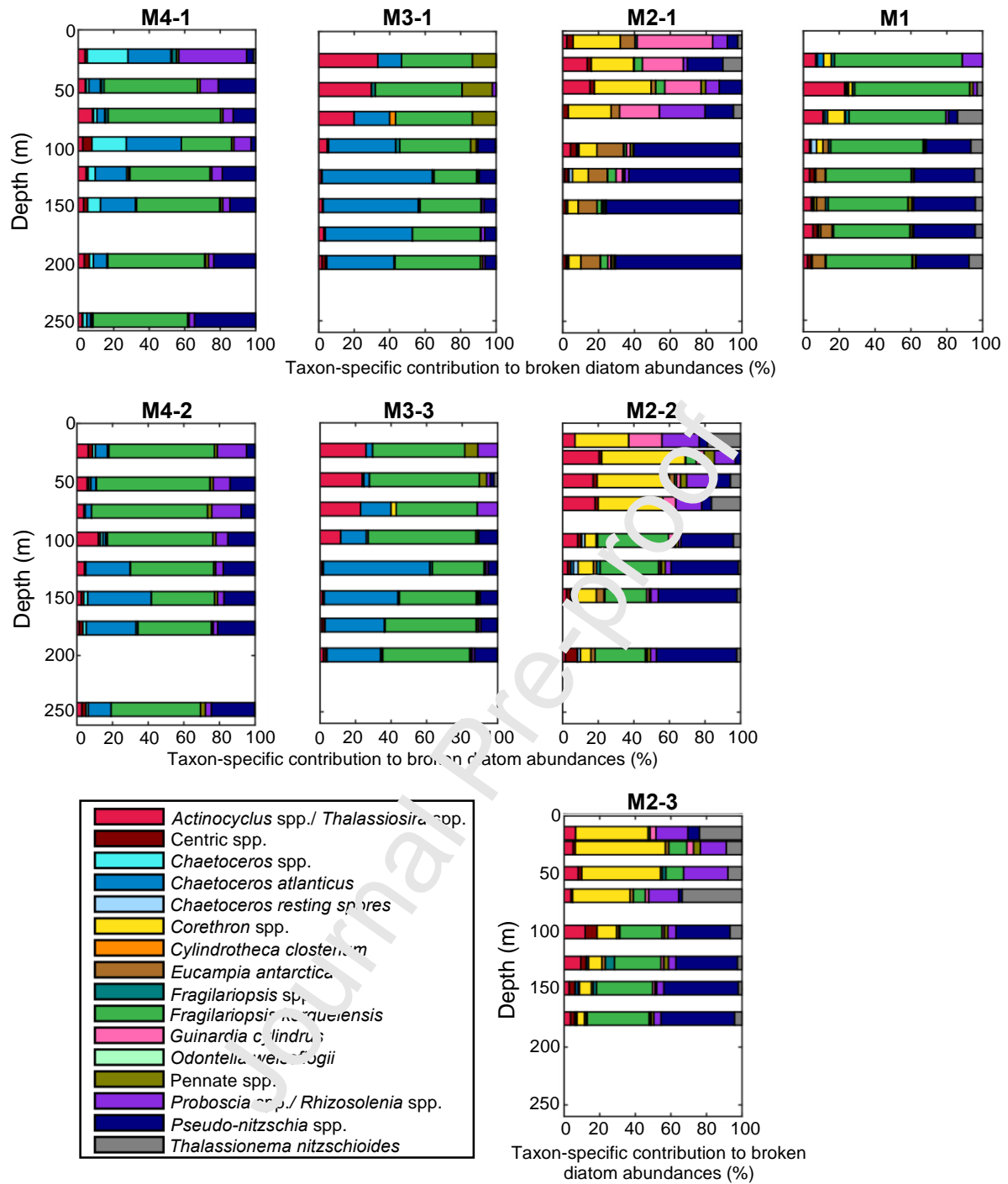


Figure S7. Taxon-specific contribution to broken diatom abundances at the four stations.

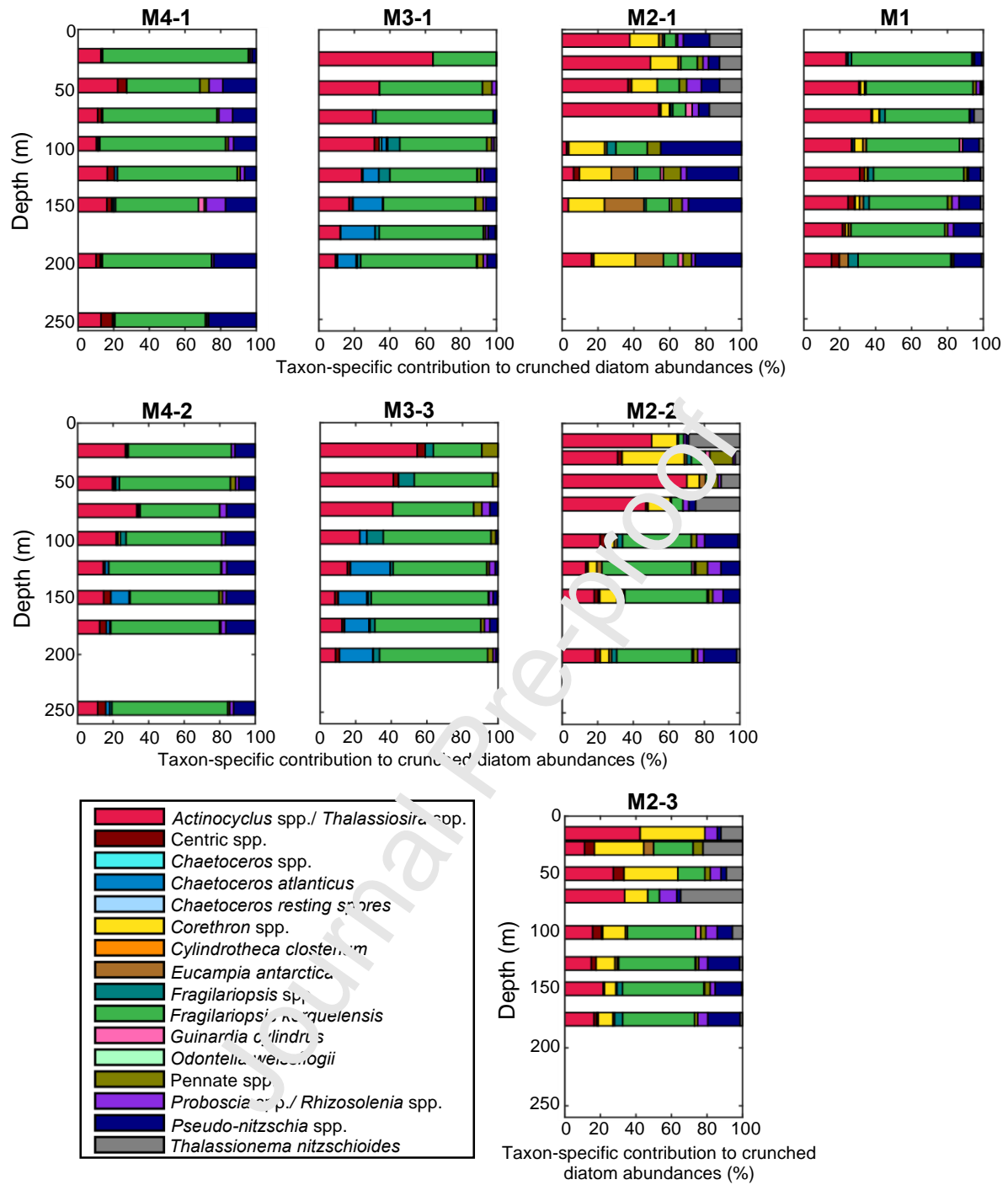


Figure S8. Taxon-specific contribution to crunched diatom abundances at the four stations.

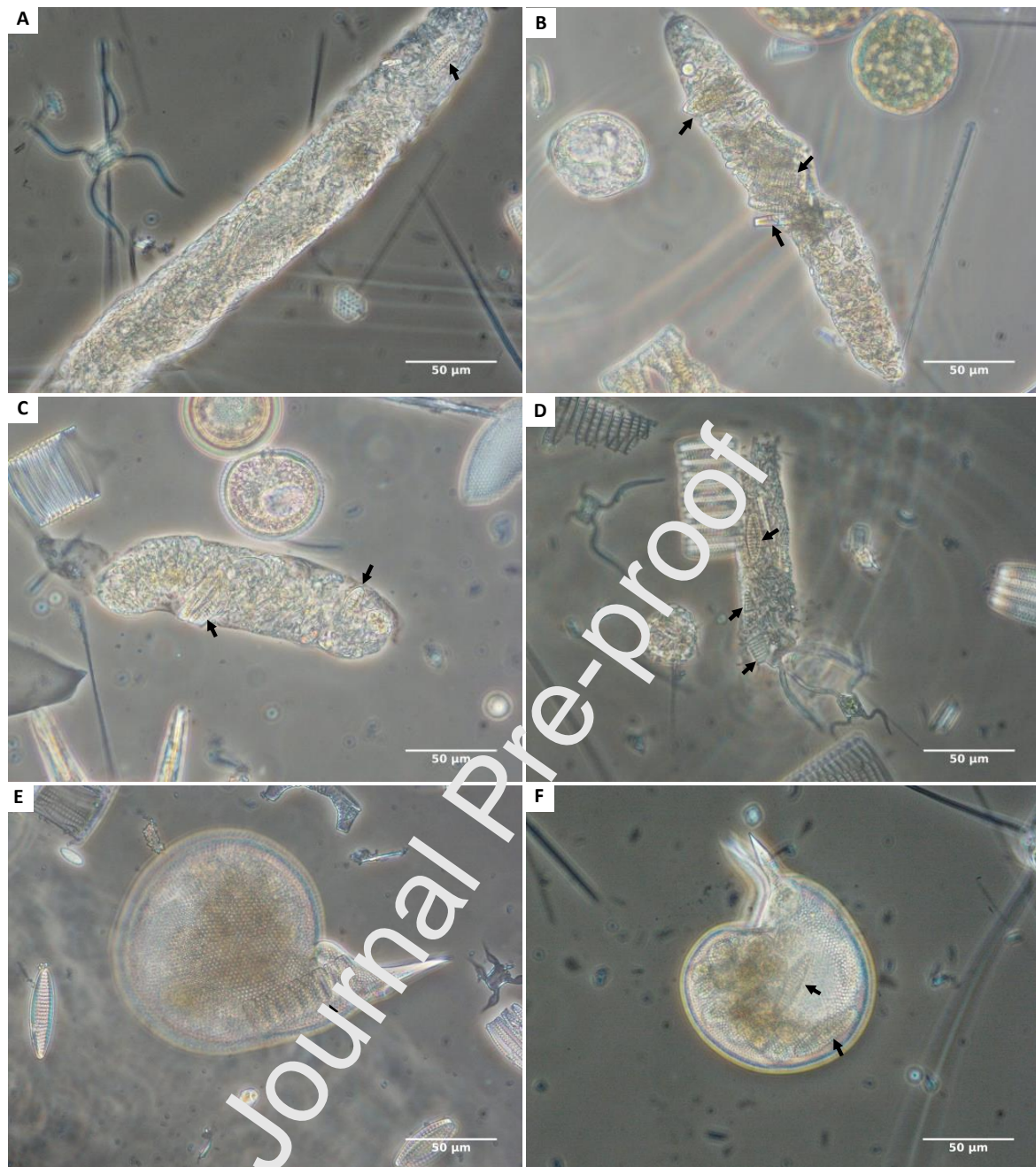


Figure S9. Selection of images evidencing grazing of the heavily silicified species *Fagilariopsis kerguelensis* by micro- and mesozooplankton, a diatom species traditionally considered as resistant to grazing. (A-D) Fecal pellets containing recognizable *F. kerguelensis* remains. *Protocystis harstoni* feeding on a whole chain (E) or solitary frustules (F) of *F. kerguelensis*. Black arrows indicate *F. kerguelensis* frustules.

Highlights

- A distinct diatom community was growing despite low $[\text{Si}(\text{OH})_4]$ above the Fe-fertilized plateau.
- A deep and inactive diatom community was systematically found within the pycnocline gradient.
- In HNLC waters, diatoms were more heavily silicified and exhibited higher Si:C ratios.
- In HNLC waters, detrital frustules of *Fragilariopsis kerguelensis* carried mostly Si below the ML.
- Above the plateau, *Chaetoceros* spp. vegetative cells and spores carried Si and C below the ML.